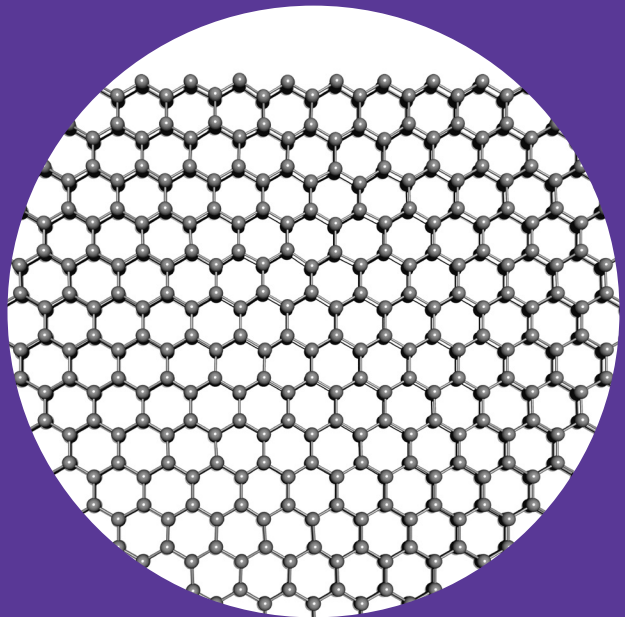


Modification of the electronic structure of graphene by quantum confinement and molecular self- assembly

Sampsa Hämäläinen



Modification of the electronic structure of graphene by quantum confinement and molecular self-assembly

Sampsa Hämäläinen

A doctoral dissertation completed for the degree of Doctor of Science (Technology) to be defended, with the permission of the Aalto University School of Science, at a public examination held at the lecture hall M1 of the school on the 31st of October 2014 at 12.

**Aalto University
School of Science
Department of Applied Physics**

Supervising professor

Professor Peter Liljeroth

Thesis advisors

Dr. Jani Sainio

Dr. Jouko Lahtinen

Preliminary examiners

Dr. Johann Coraux, Institut Néel, CNRS & Université Joseph Fourier,
France

Dr. Pekka Laukkanen, Materials Research Laboratory, University of
Turku, Finland

Opponent

Professor Markus Morgenstern, RWTH Aachen, Germany

Aalto University publication series

DOCTORAL DISSERTATIONS 150/2014

© Sampsa Hämäläinen

ISBN 978-952-60-5886-3

ISBN 978-952-60-5887-0 (pdf)

ISSN-L 1799-4934

ISSN 1799-4934 (printed)

ISSN 1799-4942 (pdf)

<http://urn.fi/URN:ISBN:978-952-60-5887-0>

Unigrafia Oy

Helsinki 2014

Finland



441 697
Printed matter

Author

Sampsa Hämäläinen

Name of the doctoral dissertation

Modification of the electronic structure of graphene by quantum confinement and molecular self-assembly

Publisher School of Science

Unit Department of Applied Physics

Series Aalto University publication series DOCTORAL DISSERTATIONS 150/2014

Field of research

Manuscript submitted 13 May 2014

Date of the defence 31 October 2014

Permission to publish granted (date) 10 June 2014

Language English

☐ **Monograph**

☒ **Article dissertation (summary + original articles)**

Abstract

Graphene has generated enormous interest after its discovery in 2004, both in the scientific community and recently even in industry. It has been highlighted as one of the strongest materials known with very high electrical and thermal conductivity. Much of the scientific interest in graphene is however related to its peculiar electronic structure.

The valence and conduction bands of graphene touch at single points on the corners of its Brillouin zone. Near these points the dispersion is linear which makes the charge carriers behave like relativistic Dirac fermions with zero effective mass, which leads to many of its exceptional electronic properties. Graphene has already been used to build field-effect transistors, but due to the absence of a band gap the on-off ratios are very poor. In order for graphene to be used as a replacement for silicon in future electronics, a gap would need to be opened between its valence and conduction bands.

In this thesis, two possible ways of modifying the graphene band structure are explored experimentally, namely quantum confinement and periodic potential modulations induced by self-assembled molecular layers. Quantum confinement of the graphene electronic states is studied on small graphene structures grown epitaxially on the (111) facet of iridium. The states are mapped by scanning tunneling spectroscopy and a continuum model using the Klein-Gordon equation is presented to model the states.

The self-assembly of cobalt phthalocyanines is studied first on epitaxial graphene on iridium(111) by scanning tunneling microscopy and low energy electron diffraction. The effect of substrate roughness on the self-assembly is then investigated on graphene on silicon oxide and hexagonal boron nitride. Finally, the structure of the graphene on Ir(111) model system used in many of the measurements, is studied in detail by atomic force microscopy and dynamic low energy electron diffraction.

Keywords graphene, scanning tunneling microscopy, quantum confinement, atomic force microscopy, iridium(111), Ir(111), self-assembly

ISBN (printed) 978-952-60-5886-3

ISBN (pdf) 978-952-60-5887-0

ISSN-L 1799-4934

ISSN (printed) 1799-4934

ISSN (pdf) 1799-4942

Location of publisher Helsinki

Location of printing Helsinki

Year 2014

Pages 106

urn <http://urn.fi/URN:ISBN:978-952-60-5887-0>

Tekijä

Sampsä Hämäläinen

Väitöskirjan nimi

Grafeenin elektronisen vyörakenteen muokkaaminen nanorakenteilla ja itsejärjestäytyneillä molekyylikerroksilla

Julkaisija Perustieteiden korkeakoulu**Yksikkö** Teknillisen fysiikan laitos**Sarja** Aalto University publication series DOCTORAL DISSERTATIONS 150/2014**Tutkimusala** Teknillinen fysiikka**Käsitteilyajankohdan pvm** 13.05.2014**Väitöspäivä** 31.10.2014**Julkaisuluvan myöntämispäivä** 10.06.2014**Kieli** Englanti☐ **Monografia**☒ **Yhdistelmäväitöskirja (yhteenvedo-osa + erillisartikkelit)****Tiivistelmä**

Kiinnostus grafeenia kohtaan, niin tiedeyhteisössä kuin teollisuudessaakin, on kasvanut räjähdysmäisesti vuoden 2004 jälkeen, jolloin yksittäinen hiiliatomikerros, eli grafeeni, onnistuttiin ensimmäistä kertaa eristämään grafiitista. Grafeeni on painonsa nähden maailman vahvinta ainetta ja se johtaa lämpöä ja sähköä erittäin hyvin. Suurin tieteellinen mielenkiinto grafeenia kohtaan on kuitenkin keskittynyt sen erikoiseen elektroniseen vyörakenteeseen.

Grafeenin valenssi- ja johtavuusvyöt koskettavat yksittäisissä pisteissä sen Brillouinin-vyöhykkeen kulmissa. Näiden pisteiden lähellä grafeenin dispersiorelaatio on lineaarinen, mikä saa varauksenkuljettajat käyttäytymään kuten massattomat relativistiset Diracin fermionit, mistä taas useat grafeenin poikkeukselliset sähköiset ominaisuudet ovat seurausta. Grafeenista on onnistuttu jo valmistamaan nopeita transistoreita, mutta niiden tilojen signaalien välinen suhde on hyvin pieni. Jotta grafeenia voisi käyttää piiteknologian korvaamiseen tulevaisuuden elektroniikassa, olisi grafeenin johtavuus- ja valenssivyön välille avattava aukko.

Tässä väitöskirjassa tutkitaan kokeellisesti kahta menetelmää energia-aukon avaamiseksi grafeeniin. Ensimmäisessä tutkitussa menetelmässä grafeenista kasvatetaan hyvin pieniä rakenteita, minkä seurauksena grafeenirakenteisiin syntyy partikkeli laatikossa -tyyppisiä energiatiloja. Tutkimuksessa kartoitetaan pienien grafeenirakenteiden tilatiheys kokeellisesti pyyhkäisyntunnelointimikroskopian avulla ja verrataan mitattuja tiloja Klein-Gordonin yhtälöstä ratkaistuihin tiloihin.

Toisessa esitetyssä menetelmässä pyritään muokkaamaan grafeenin vyörakennetta itsejärjestäytyvän molekyylikerroksen aikaansaamalla jaksollisella potentiaalimodulaatiolla. Molekyylien järjestymistä vertaillaan grafeeninäytteillä eri substraateilla, joiden pinnoilla grafeenilla on eri karkeus. Koska suuri osa mittauksista on tehty iridium yksittäiskiteelle kasvatetulle epitaksiaalisella grafeenilla, on osa tukimuksesta keskittynyt grafeenin rakenteen tutkimiseen kyseisellä pinnalla atomivoimamikroskopian ja matalaenergisten elektronien diffraktion avulla.

Avainsanat grafeeni, pyyhkäisyntunnelointimikroskopia, atomivoimamikroskopia, grafeeninanorakenteet, iridium, itsejärjestäytyminen

ISBN (painettu) 978-952-60-5886-3**ISBN (pdf)** 978-952-60-5887-0**ISSN-L** 1799-4934**ISSN (painettu)** 1799-4934**ISSN (pdf)** 1799-4942**Julkaisupaikka** Helsinki**Painopaikka** Helsinki**Vuosi** 2014**Sivumäärä** 106**urn** <http://urn.fi/URN:ISBN:978-952-60-5887-0>

Preface

Looking back on when I started to work on this thesis, I can now say that I had no idea what I was getting myself into. Luckily I have had several great people to help me out along the way, whom I now wish to thank.

First of all I would like to thank Dr. Jouko Lahtinen for giving me the opportunity to start working towards a doctoral degree in the the first place. I started my work in the Surface Science group on the then newly acquired scanning tunneling microscope (STM). As I guess is often the case in experimental research, things do not always work out perfectly, or at least not as planned. In my case this meant broken microscopes, leaking vacuum chambers and me spending the first few years of my PhD studies just trying to get things working in the lab. During this time I was helped enormously by my thesis advisor Dr. Jani Sainio, whose motto of "leading from the front" meant that I was never left alone with the wrench in the lab, but always had a pair of extra hands to help me out.

In addition to teaching me a lot about the machines I was working with, the problems in the lab lead Jouko to introduce me to Dr. Peter Liljeroth, at the time a visiting researcher from the University of Utrecht, who later became Prof. Peter Liljeroth and the supervisor of my thesis. Peter's general enthusiasm and especially his knowledge on scanning probe techniques was what really got my scientific work started, and kept it going.

As we still had problems with our microscope in Helsinki, Peter organized for me to visit Daniël Vanmaekelbergh's group in the University of Utrecht who at the time had a very nice microscope setup. This started a very fruitful Dutch-Finnish collaboration which still goes on, and has resulted in the majority of the papers included in this thesis. I am very thankful to Daniël for letting me visit their group on so many occasions. I also want thank all the people in the group for always making me feel like home when visiting Utrecht, especially Zhixiang, Mark and Joost who al-

ways helped me out with everything both in and outside the lab and often spent long days (nights) in the lab helping me get all my measurements done before I had to leave back to Finland.

From Aalto University, I would like to thank Dr. Ari Harju, Dr. Mari Ijäs and Dr. Andreas Uppstu from the Quantum Many-Body Physics group, for the numerous times they have helped me understand our measurements. I also want to acknowledge all the members of the Atomic Scale Physics group, whom I have enjoyed working with for the past years; Päivi, Robert, Kaustuv, Fabian, Avijit, Shawulienu and Amina, Thanks for the fun times.

Finally, I want to thank my family and friends for always being there to keep my mind off work when this was needed.

Helsinki, September 23, 2014,

Sampsa Hämäläinen

Contents

Preface	i
Contents	iii
List of Publications	v
Author's Contribution	vii
1. Introduction	1
2. Experimental methods	7
2.1 Graphene growth by chemical vapor deposition on iridium .	7
2.2 Scanning tunneling microscopy	10
2.2.1 Basic principle and imaging	10
2.2.2 Tunneling spectroscopy	13
2.3 Non-contact atomic force microscopy	16
2.4 Low-energy electron diffraction (LEED)	20
2.4.1 Single scattering and the Bragg condition	20
2.4.2 Multiple scattering - Dynamic LEED (LEED-I(V)) . .	22
3. Results	25
3.1 Structure of epitaxial graphene on Ir(111)	25
3.2 Confined electronic states in graphene	31
3.3 Molecular self-assembly on graphene	37
4. Summary and outlook	43
Bibliography	45
Errata	55
Publications	57

List of Publications

This thesis consists of an overview and of the following publications which are referred to in the text by their Roman numerals.

I Zhixiang Sun, Sampsa K. Hämäläinen, Jani Sainio, Jouko Lahtinen, Daniël Vanmaekelbergh, Peter Liljeroth. Topographic and electronic contrast of the graphene moiré on Ir (111) probed by scanning tunneling microscopy and noncontact atomic force microscopy. *Physical Review B*, 83, 081415(R), 2011.

II Sampsa K. Hämäläinen, Zhixiang Sun, Mark P. Boneschanscher, Andreas Uppstu, Mari Ijäs, Ari Harju, Daniël Vanmaekelbergh, Peter Liljeroth. Quantum-Confined Electronic States in Atomically Well-Defined Graphene Nanostructures. *Physical Review Letters*, 107, 236803, 2011.

III Sampsa K. Hämäläinen, Mariia Morozova, Robert Drost, Peter Liljeroth, Jouko Lahtinen, Jani Sainio. Self-Assembly of Cobalt-Phthalocyanine Molecules on Epitaxial Graphene on Ir(111). *Journal of Physical Chemistry C*, 116, 20433-20437, 2012.

IV Päivi Järvinen, Sampsa K. Hämäläinen, Kaustuv Banerjee, Pasi Häkkinen, Mari Ijäs, Ari Harju, Peter Liljeroth. Molecular self-assembly on graphene on SiO₂ and h-BN substrates. *Nano Letters*, 13, 3199-3204, 2013.

V Sampsa K. Hämäläinen, Mark P. Boneschanscher, Peter H. Jacobse, Ingmar Swart, Katariina Pussi, Wolfgang Moritz, Jouko Lahtinen, Peter

Liljeroth, Jani Sainio. Structure and local variations of the graphene moiré on Ir(111). *Physical Review B*, 88, 201406(R), 2013.

Author's Contribution

Publication I: “Topographic and electronic contrast of the graphene moiré on Ir (111) probed by scanning tunneling microscopy and noncontact atomic force microscopy”

The author took part in the scanning probe measurements, derived the theoretical model for the tip-sample interaction and wrote the theoretical part of the article.

Publication II: “Quantum-Confined Electronic States in Atomically Well-Defined Graphene Nanostructures”

The author did the scanning tunneling spectroscopy measurements and the finite element method modeling of the graphene quantum dot eigenstates by the Klein-Gordon equation and wrote the first version of the manuscript.

Publication III: “Self-Assembly of Cobalt-Phthalocyanine Molecules on Epitaxial Graphene on Ir(111)”

The author conducted the scanning tunneling microscopy and low-energy electron diffraction experiments and wrote the paper.

Publication IV: “Molecular self-assembly on graphene on SiO₂ and h-BN substrates”

The author carried out some of the experiments and took part in analyzing the data and writing the paper.

Publication V: “Structure and local variations of the graphene moiré on Ir(111)”

The author planned the experiment, measured the low-energy electron diffraction data, analyzed the atomic force microscopy measurements and wrote the paper.

1. Introduction

Much of the materials research in recent years has focused on nanomaterials. These are materials whose physical properties differ from their bulk counterparts due to their small size. One of the most interesting groups of such materials is based on the hexagonal structure of a single graphite layer, or graphene. By folding a graphite layer, one can produce either ball-like fullerenes¹ or tubular carbon nanotubes.² Interestingly, graphene, the building block of the former structures, was the last one to gain the interest of the scientific community. After the groundbreaking experiments on graphene in 2004 by Andre Geim and Konstantin Novoselov,³⁻⁷ which later won them the Nobel Prize in Physics, the interest in graphene has exploded.

Apart from graphene's unique mechanical and optical properties,⁸ it is the electronic band structure of graphene which is driving much of the research. Graphene is formed by sp^2 bound carbon atoms in a honeycomb lattice (fig. 1.1). The p_z orbitals are not involved in the sigma bonding of the graphene backbone and make up the π -bands that form the con-

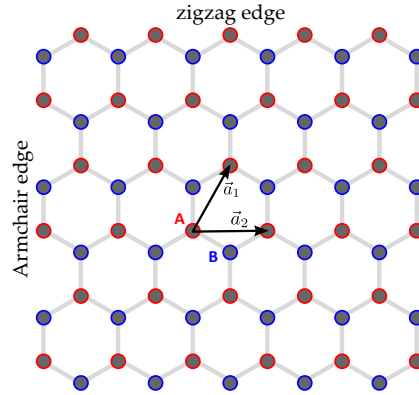


Figure 1.1. Illustration of the structure of graphene. The two carbon sublattices (labeled A and B) are equivalent.

duction and valence bands of graphene. The primitive unit cell is formed by two equivalent sublattices noted by A and B in figure 1.1. This symmetry of the two sublattices is what gives rise to graphene's distinctive band structure. Graphene is a semi-metal, i.e the valence and conduction bands touch at a single point on the corners of its Brillouin zone (fig. 1.2). Near this crossing these π -bands are linear, which results in the charge carriers (electrons and holes) to have zero effective mass.⁹ This along with the sublattice symmetry makes low energy excitations in graphene behave like relativistic Dirac fermions which satisfy the Dirac equation for massless particles

$$-i\hbar v_F \begin{pmatrix} 0 & (\partial_x - \partial_y) \\ (\partial_x + \partial_y) & 0 \end{pmatrix} \begin{pmatrix} \psi_a \\ \psi_b \end{pmatrix} = E \begin{pmatrix} \psi_a \\ \psi_b \end{pmatrix}, \quad (1.1)$$

where the two off diagonal elements in the Hamiltonian are momentum operators in the graphene plane and ψ_a and ψ_b the electron wave functions of the two sublattices. The Fermi velocity v_F defines the constant velocity with which the charge carriers move and is around 10^6 m/s for freestanding graphene. The fact that the Hamiltonian for the electronic excitations in graphene takes the form of the Dirac Hamiltonian gives rise to a plethora of interesting phenomena which cannot be observed in most other materials, such as the anomalous quantum Hall effect,^{6,10,11} Klein tunneling¹² and the pseudospin^{12–14} oppositely aligned with the momentum in the two valleys in the Brillouin zone (marked by K and K' in the band structure in fig. 1.2).

What is interesting to note is that an analogous band structure exhibiting the same physical phenomena as graphene will result from any two-dimensional honeycomb structure where the two sublattices are symmetric. In other words, the magic is not in the carbon atoms themselves but in the way they can be bound together into a honeycomb lattice. Engineering a similar two-dimensional structure from some other element would yield a very similar band structure. This was very nicely demonstrated by locally quenching the copper (111) surface state by carbon monoxide molecules to form a honeycomb lattice where the surface state could live.¹⁵ The authors showed that the quasiparticle excitations in the patterned surface state follow the Dirac equation while the Fermi velocity and doping of this pseudographene could be manipulated by slight changes in the patterning of the adsorbed CO molecules.

One interesting practical property of graphene is its charge carrier mobility. Back scattering of charge carriers in graphene would require scat-

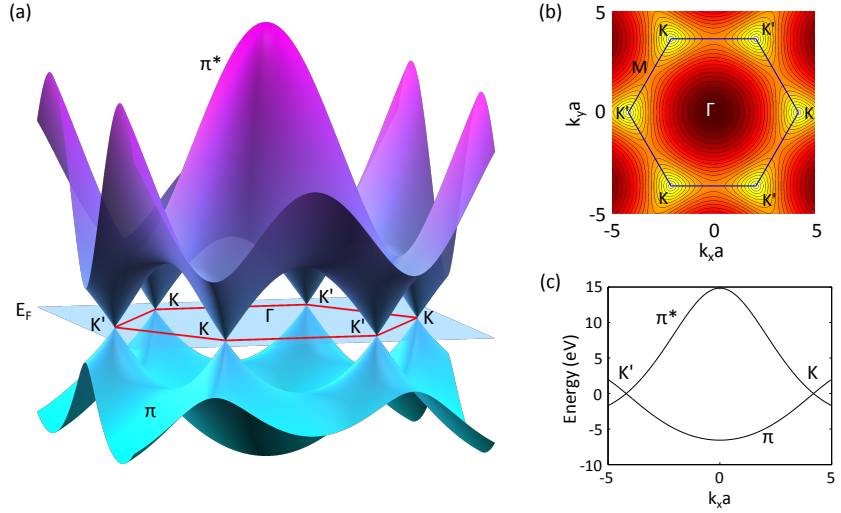


Figure 1.2. (a) Dispersion of the graphene π and π^* bands calculated from the nearest-neighbor tight binding model. The red hexagon represents the 1st Brillouin zone and the blue plane the Fermi level E_F . (b) The π -band of graphene showing the two valleys denoted by K and K'. (c) A cut out across through the Brillouin zone from K' to K.

tering between the two valleys in the band structure, i.e. K and K' in figure 1.2. This would essentially require the pseudospin of the state to change sign and therefore scattering is suppressed. Hence, charge carrier mobilities in graphene are very high even at room temperature.^{3,16} From an electronics point of view this is a very attractive property for a material, especially for transistors. In radio frequency (RF) transistors, the capacitance of the circuit needs to be charged and discharged through the channel during every cycle. This capacitance is what limits the switching rate of the circuit. As transistors with higher mobility will produce higher currents through the channel to charge the capacitance quicker, the clock rates of such transistors can be pushed to higher frequencies.

Most of today's transistors are manufactured from silicon which is a semiconductor with a band gap of 1.1 V. The band gap is needed in order to be able to switch the current through the transistor on and off for performing logical operations. As a semi-metal graphene has no band gap, hence a transistor made out of graphene as such can never be turned to a complete off-state. If graphene is to become the future material of electronics, a way to open a band gap and control the Fermi level, i.e. doping, needs to be established.

There are several different schemes to open a gap in the graphene band structure. The most straightforward method is through quantum confine-

ment of the electronic states. The idea in short is to make the graphene structures small enough for the states near the Fermi level to not fit in. The principle has been demonstrated to work by preparing narrow graphene ribbons (10...100 nm) by electron beam lithography and measuring electron transport through them.¹⁷⁻¹⁹

The band diagram presented in figure 1.2 describes the charge carriers in bulk graphene. In a narrow graphene ribbon, additional flat bands can appear at the Fermi level which are localized on the edge of the ribbon. Graphene edges can have two basic orientations, which are named after their appearance as *zigzag* and *armchair*. The two orientations are depicted in figure 1.1. The flat band on the edge only appears on the zigzag edge. Hence when studying small graphene structures, the edge orientation plays a crucial role. This cannot be easily controlled in the top-down approaches such as lithography which are commonly used in building graphene devices. Bottom-up approaches, such as on-surface polymerization of graphene nanoribbons,^{20,21} unzipping of nanotubes²² and controlled chemical vapor deposition,²³ offers ways to grow well defined graphene nanostructures, where the orientation of the edges is defined by the growth process.

Another way to introduce a gap is to break the sublattice symmetry in graphene.^{24,25} This will cause the charge carriers to gain mass. The Dirac equation (eq. 1.1) can be used to describe these massive particles. The zeros on the diagonal of the Hamiltonian are in this case replaced by $\pm v_F m^*$, where m^* is the effective mass of the particle. The inclusion of mass results in a hyperbolic dispersion relation around the Dirac points and the opening of a gap between the valence and conduction bands. Massive Dirac fermions in graphene were recently demonstrated experimentally by placing graphene on top of hexagonal boron nitride so that the two lattices are aligned. This locally breaks the sublattice symmetry and leads to alternating regions of positive and negative effective mass.²⁶

The graphene band structure can be altered without the aim of opening a gap as well. In pristine graphene the Dirac cones near the Fermi level are symmetric. By introducing a periodic potential modulation in the graphene sheet, the symmetry can however be reshaped producing oval shaped cones.^{27,28} This allows one to tune the Fermi velocity of the charge carriers in graphene in a way that depends on the direction of the momentum of the charge carriers.

In this thesis, methods to engineer the graphene band structure are

studied experimentally using scanning probe microscopy and low energy electron diffraction. Chapter 2 presents the method of graphene growth on iridium and the experimental techniques used in the Publications. Chapter 3 reviews the main results from the publications and the work is finally summarized in Chapter 4.

2. Experimental methods

2.1 Graphene growth by chemical vapor deposition on iridium

Graphene can be produced by several different methods. In their Nobel price winning experiments, Geim and Novoselov isolated graphene by exfoliation from graphite using standard Scotch tape. The method produces high quality graphene but in rather small sized flakes and heavily relies on trial and error and searching to find the single layer graphene flakes among the multilayer flakes.²⁹ A more scalable process for graphene production is to grow it by chemical vapor deposition (CVD) on a metal substrate. In CVD growth, the metal substrate is heated to a high temperature in an atmosphere of a carbon containing precursor gas such as ethylene or methane. The precursor cracks on the hot surface leaving carbon on the surface which then forms the graphene layer. The method can be used on a wide range of transition metals,^{30,31} e.g. Cu,^{32,33} Pt,^{34–36} Fe,³⁷ Ni,³⁸ Pd,^{39,40} Ir,^{23,34,41} Re,^{42,43} Ru,^{44–46} Rh^{44,47} and Co.^{48,49} Depending on the solubility of carbon in the metal, the growth proceeds either directly by carbon diffusion on the surface or through carbon dissolution into the bulk and segregation back to the surface while cooling the crystal down, or through a combination of the two. When direct surface diffusion is the dominant growth route, the process is self-limiting to a single layer as the bare metal is required for the cracking of the precursor.

For most of the substrates the growth can be carried out on both single crystals and metal foils in either ultra-high vacuum (UHV) chambers or in ambient pressure furnaces. Recently similar approaches to the CVD method have been shown to work even on non-metallic substrates, such as germanium⁵⁰ and hexagonal boron nitride.^{51,52}

The (111) facet of iridium has become one of the most popular substrates

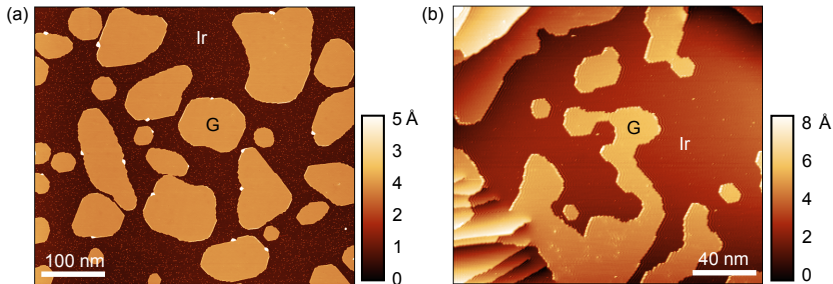


Figure 2.1. Scanning tunneling microscopy images of graphene islands grown on iridium by pre-adsorbing ethylene and annealing at 1470 K.

for graphene growth in UHV studies. Typically the precursor used is ethylene but many other hydrocarbons work just as well. The reasons why Ir(111) is such a popular substrate are related to both the growth process and the properties of the resulting graphene layer. The growth mode on iridium is dominated by surface diffusion and hence the graphene growth is automatically limited to a single layer as breaking of the carbon precursor is catalyzed by the metal surface. The interaction between graphene and iridium is also very nicely balanced; it is weak enough to let the Dirac cones in the band structure survive,⁵³ yet it is strong enough to result in a preferential growth direction so that very large defect free single-domain islands can be grown.^{23,54,55}

There are two principle ways of growing graphene on Ir(111) from ethylene depending on the point at which the crystal is heated. The ethylene can either be introduced directly on the hot substrate where it cracks and forms graphene or the ethylene may first be adsorbed on the Ir(111) substrate at room temperature and heated afterwards.²³ The former method is a simple way to get a full coverage of graphene but requires some calibration if sub-monolayer coverages are desired. The pre-adsorption method, or temperature programmed growth (TPG) as it is also called, on the other hand allows considerably better control over the size and coverage of the graphene grown.

Adsorption of ethylene on Ir(111), like most gases on metals, is self-limiting to a single layer. Upon adsorption at room temperature, one hydrogen is released from the ethylene molecule to form ethylidyne.^{56,57} By heating the substrate the ethylidyne further dehydrogenates and at around 800 K only carbon is left on the surface in various forms.³⁴ Soon after this while increasing the temperature, the carbon on the surface will already start forming small graphene islands.^{23,34} The coverage of graphene in the end is limited by the amount of carbon on the surface

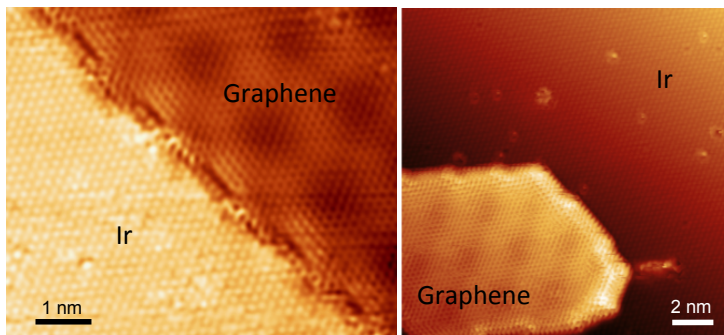


Figure 2.2. Atomically resolved STM images of graphene on Ir showing the alignment of the two lattices.

before heating. Since the carbon atom density in the ethynidyne layer is well-defined and lower than in graphene, the method always produces roughly the same graphene coverage of around 22 %.²³ Depending on the temperature and length of the annealing, the method can be used to produce graphene islands of various sizes. At the growth temperature of around 1000...1500 K whole graphene islands will diffuse and coalesce forming larger and larger islands. Figure 2.1 shows STM images of graphene grown by pre adsorption of ethylene. In figure 2.1b the long structures are formed through the aforementioned diffusion of intact graphene islands, i.e. Smoluchowski ripening. For extended annealing periods at even higher temperatures, the grain boundaries formed by the Smoluchowski ripening will slowly disappear.

Almost all the graphene islands grown by the preadsorption of ethylene have their lattice roughly aligned with the underlying iridium substrate. This can be seen in the atomically resolved STM images of a graphene island growing out of an iridium step edge and an isolated graphene island in figure 2.2. Another feature of graphene grown on iridium is that all of the free graphene edges are terminated in the zigzag direction of the graphene lattice and all corners on the edge of the graphene are 120° .

The superstructure visible on graphene in figure 2.2 is the moiré pattern produced by the mismatch between the surface lattice constants of graphite (2.461 Å) and iridium (2.715 Å).⁵⁸ A moiré pattern is essentially the interference pattern formed between two slightly different frequencies. It is commonly observed in sound as a beating pattern when tuning an instrument or in digital photography of fine structures at the scale of the pixels in the camera sensor. Figure 2.3 shows an example of a honeycomb lattice placed on top of a hexagonal lattice with slightly different

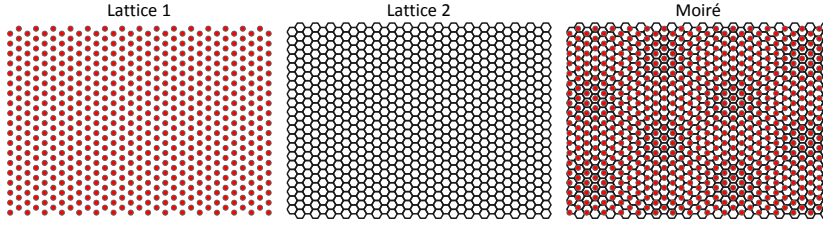


Figure 2.3. The resulting moiré pattern produced by placing a honeycomb lattice on top of a hexagonal lattice.

lattice constants forming a moiré pattern. Mathematically the reciprocal lattice constant of a moiré pattern is given by the difference of the reciprocal lattice vectors,⁵⁹ i.e.

$$\vec{k}_{moire} = \vec{k}_1 - \vec{k}_2. \quad (2.1)$$

As is evident from equation 2.1, the period and direction of the moiré pattern also depend on the rotation of the graphene lattice with respect to the iridium lattice. For a hexagonal lattice with lattice constant a and an substrate with a lattice mismatch δ , the wave length, or period, of the moiré pattern can be derived from 2.1 to give⁶⁰

$$\lambda = \frac{(1 + \delta)a}{\sqrt{2(1 + \delta)(1 - \cos\phi) + \delta^2}}, \quad (2.2)$$

ϕ is the angle between the two lattices. The angle of the moiré pattern with respect to the overlayer lattice is then given by

$$\tan\theta = \frac{\sin\phi}{1 + \delta - \cos\phi}. \quad (2.3)$$

For small angles of graphene on Ir(111), equation 2.3 gives a roughly 10 fold magnification of the angle between the graphene and Ir lattices, i.e. if the graphene lattice is rotated by ϕ with respect to the Ir(111) lattice, the moiré will be rotated by 10ϕ .⁵⁸

2.2 Scanning tunneling microscopy

2.2.1 Basic principle and imaging

STM is one of the few methods by which individual atoms can be directly imaged and manipulated. It was invented in the early 80s at the IBM Zürich Laboratory by Gerd Binnig and Heinrich Rohrer,^{61–63} who were later in 1986 acknowledged for their invention with the Nobel Prize in

Physics. Today STM is a well-established method with several commercial companies producing ready to use systems.

As its name suggests the basic operating principle is based on the quantum mechanical phenomenon of tunneling. The imaging in STM is done by a thin metal wire which is brought close to the sample surface. The sample is biased with respect to the tip and the tip is raster scanned over the sample surface. The layer of air or vacuum between the tip and sample acts as a barrier for the electrons. Unlike in classical physics, where the electron cannot travel through the barrier in quantum mechanics so called quantum tunneling is allowed. In quantum mechanics the electron is described by a wave function $\psi(x)$, which satisfies the Schrödinger equation. The probability of finding the electron at point x is given by the square of the wave function. For the time-independent one-dimensional case of the potential barrier between the tip and sample, the Schrödinger equation can be written as

$$-\frac{\hbar^2}{2m} \frac{d^2}{dx^2} \psi(x) + U(x)\psi(x) = E\psi(x), \quad (2.4)$$

where \hbar is the reduced Planck constant, m the mass of the electron, x the position, $U(x)$ the potential along x and E the energy of the electron. In the case of the potential barrier presented in figure 2.4, the Schrödinger equation has two different types of solutions. The solutions in the classically allowed regions outside the barrier ($E > U$) are plane waves of the form

$$\psi(x) = \psi(0)e^{\pm ikx}, \quad (2.5)$$

where k is the wave vector, given by

$$k = \frac{\sqrt{2m(E - U)}}{\hbar}. \quad (2.6)$$

The signs in 2.5 refer to the direction of the plane wave. Equation 2.4 can also be solved inside the classically forbidden region in the barrier. The solution in the barrier is an exponentially decaying curve which for the electron going in the positive direction in x is

$$\psi(x) = \psi(0)e^{-\kappa x}, \quad (2.7)$$

where the decay constant κ is given by

$$\kappa = \frac{\sqrt{2m(U - E)}}{\hbar}. \quad (2.8)$$

Taking the square of equation 2.7

$$\frac{|\psi(x)|^2}{|\psi(0)|^2} = e^{-2\kappa x} \quad (2.9)$$

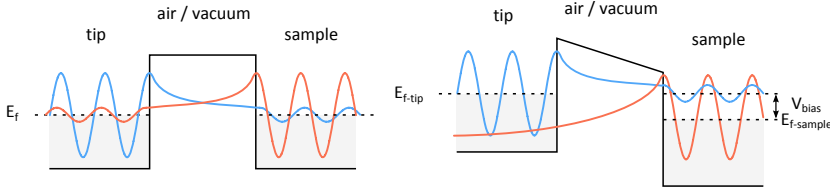


Figure 2.4. Simplified model for the tunnel junction between the STM tip and the sample for a hypothetical system with a constant density of states. On the left no bias is applied and on the right a small bias is applied between the sample and tip. The blue line presents a plane wave type electron wave function tunneling from the tip to the sample and the red curve from sample to tip.

gives the probability of finding the electron behind a barrier of width x , and the tunneling current I can be written as

$$I = I_0 e^{-2\kappa x}, \quad (2.10)$$

where I_0 is a constant. In the case where the Fermi levels on either side of the barrier are aligned (fig. 2.4 left panel), no net current will flow through the barrier as it is equally likely for the electron to tunnel left and right. By applying a voltage difference over the barrier (fig. 2.4 right panel) this is changed. Now there are no states on the left hand side of the barrier for the electron on the right (red curve) to tunnel to and hence the wave function keeps decaying exponentially even behind the barrier. The electron on the left hand side (blue curve) can still tunnel through and hence a net current will flow through the tunneling barrier.

The vacuum barrier between the metal tip and sample in STM can be approximated with the work function of the tip (or sample). Plugging typical values of the work function (3...6 eV) in equation 2.8 gives a κ of around 1 \AA^{-1} . What this means is that the tunneling current is very sensitive to the barrier width, i.e. tip-sample distance. The current falls by an order of magnitude for every Ångström the distance is increased.

In STM, the short decay length of the tunneling current is used as a measure of the tip-sample distance. In the most commonly used imaging mode, the constant current mode, the tip is raster scanned over the surface while a feedback loop keeps the tunneling current constant by adjusting the tip-sample distance (see fig. 2.5). The feedback output, i.e. the movement of the tip in the z-direction, is recorded and gives the real space topography over the raster scanned area.

It goes without saying that in order for the above scheme to work the tip needs to be moved very accurately both vertically and laterally. This is achieved by moving the tip or sample with piezoelectric crystals. The

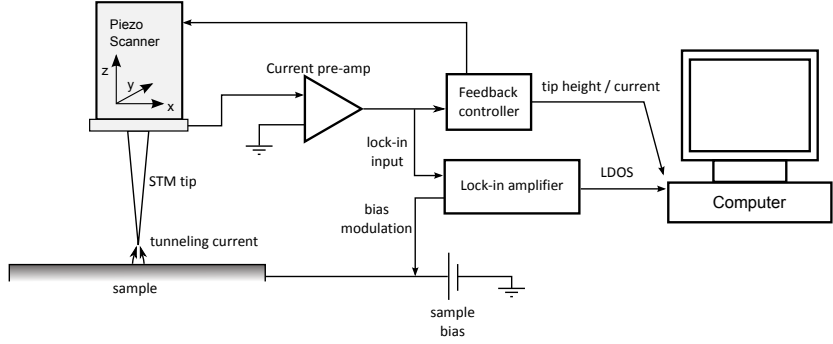


Figure 2.5. Schematic drawing of a scanning tunneling microscope equipped with a lock-in amplifier for measuring the local density of states (LDOS).

lattice strain in a piezo crystal can be controlled by an external electric field. Hence by adjusting the electric field the dimensions of the crystal can be changed. The most common way to implement the tip/sample movement using piezoelectric crystals is a piezo tube, where the outside of the piezo tube is divided into quadrants with indecent electrodes that are biased against a common center electrode. This allows the tube to be bent sideways and extended and retracted while maintaining a single piece of crystal for stability and simplicity. Hence the single block can take care of all the movements required in an STM.

2.2.2 Tunneling spectroscopy

The tunneling current is not only dependent on the barrier width, i.e. tip-sample distance, but also depends on the density of available electronic states to tunnel to. Hence the STM image does not represent the true topography of the surface, but is rather a convolution of the topography and local density of states (LDOS) on the surface. Assuming that the bias is applied to the sample, then a positive bias will have electrons tunneling from the tip to the sample and a negative bias from the sample to the tip. For a positive sample bias V_b , the tip electrons with energy above $(E_{F-tip} - eV_b)$ can tunnel to any of the unoccupied sample states below $(E_{F-sample} + eV_b)$, where E_{F-tip} and $E_{F-sample}$ are the Fermi levels of the tip and sample, respectively. The tunneling current is then proportional to the sum of all the states in this interval. i.e.

$$I \propto \int_0^{eV_b} \rho_{sample}(E_F - eV_b + \epsilon) \rho_{tip}(E_F + \epsilon) d\epsilon, \quad (2.11)$$

where ρ_{sample} and ρ_{tip} are the sample and tip density of states at a given energy and E_F the tip Fermi level. Equation 2.11 assumes that the tun-

neling probability between all states is equal. In reality this is not the case as the overlap of the tip and sample orbitals can vary significantly. This can be taken into account using the so called tunneling matrix M which gives the probability of an electron to tunnel between two states

$$I = \int_0^{eV_b} \rho_{sample}(E_F - eV_b + \epsilon) \rho_{tip}(E_F + \epsilon) |M|^2 d\epsilon. \quad (2.12)$$

Assuming that for a metallic tip the density of states is flat, and that the tunneling matrix does not change much in a small energy window, the tunneling current becomes proportional to the integral over the sample states. The integral can then be separated and the sample local density of states at a given energy becomes proportional to the differential conductance of the tunneling junction at that energy

$$I \propto \int_0^{eV_b} \rho_{sample}(E_F - eV_b + \epsilon) d\epsilon \implies \rho_{sample}(eV_b) \propto \frac{dI(V_b)}{dV_b} \quad (2.13)$$

Hence STM can be used to probe the LDOS of the sample under the tip by measuring the differential conductance. This can be done by measuring the tunneling current as a function of sample bias and differentiating the resulting curve, or the differentiation can be done directly during the experiment using a lock-in amplifier (see fig. 2.5). The output of the lock-in amplifier is used to modulate the sample bias, typically with an amplitude of some tens of millivolts. The tunneling current signal is then connected to the lock-in input and demodulated at the same frequency as the output. The amplitude of the demodulated tunneling current directly gives the differential conductance.

The LDOS can be measured in a single point as a function of bias as explained above or mapped at a certain bias. In the case of point spectra, the z-feedback is usually turned off for the measurement whereas mapping can either be done at constant height (feedback off) or at constant current (feedback on). If the feedback is kept on, the bias modulation frequency must be higher than the bandwidth of the z-feedback loop, not to couple the modulation to the vertical position of the tip. The frequency of the bias modulation must at the same time remain below the bandwidth of the current preamplifier, which in typical STM setups is around 1 kHz. Due to these limitations, the modulation frequency is usually chosen around 400...1000 Hz.

Depending on whether the feedback loop is open (constant height) or closed (constant current), the measured signal can differ significantly on certain samples. When measuring spectra at a single point as a function

of bias, the measured differential conductance can be normalized by I/V_b in order to try to cancel out the dependence of the tunneling barrier on V_b .^{64–66} When mapping dI/dV_b in constant current mode the measured differential conductance is actually proportional to the normalized signal $(dI/dV_b)/(I/V_b)$ as the feedback keeps I constant and V_b is constant by definition. Hence it would seem natural to take the dI/dV_b measured at constant current to represent the LDOS. The problem is that in constant current mode the tip height relative to the sample changes depending on the *integral* of the density of states between 0 V and V_b . Hence all the lower energy states couple to the dI/dV_b signal measured at V_b through the variation in the barrier width caused by the feedback. On samples with large variations in the LDOS this can lead to significantly skewed LDOS maps.⁶⁷

In addition to probing the LDOS, STM can also be used to probe the local barrier height through the decay constant κ . Making the simple assumption that the tunneling barrier height U is equal to the average of the sample and tip barrier heights Φ and that the bias used is much lower than Φ , equation 2.8 can be written as

$$\kappa = \frac{\sqrt{2m\Phi}}{\hbar} \implies \Phi = \frac{2m\kappa^2}{\hbar^2} \quad (2.14)$$

The decay constant can be easily obtained on different points of the sample by measuring the tunneling current as a function of tip height and plotting the logarithm of the current as a function of tip height. The slope of the plotted curve then gives -2κ from which the average barrier height Φ can be calculated.

A similar lock-in amplifier scheme to the one used in LDOS maps can also be used to map the barrier height. The lock-in amplifier output modulation is now connected to the z-piezo, effectively shaking the tip up and down with an amplitude of some tens of picometers. The current is again demodulated and by assuming a small oscillation amplitude the lock-in signal can be approximated to be proportional to the derivative of the current with respect to the tip height. Taking the derivative of the tunneling current given by eq. 2.10 with respect to the tip height z gives

$$\frac{dI}{dz} = -2\kappa I_0 e^{-2\kappa z} = -2\kappa I, \quad (2.15)$$

where I is the average tunneling current defined by the feedback set point. Multiplying eq. 2.15 by the modulation amplitude Δz will give the amplitude of the demodulated signal on the lock-in input, from which κ can be

solved

$$I_{lock-in} = 2\kappa\Delta z I \implies \kappa = \frac{1}{2\Delta z} \frac{I_{lock-in}}{I} \quad (2.16)$$

The average work function can then be solved by combining equations 2.14 and 2.16.

$$\Phi = \frac{m}{2\hbar^2\Delta z^2} \left(\frac{I_{lock-in}}{I} \right)^2 \quad (2.17)$$

Since the above relation depends on I , it is practical to do the measurement with the feedback loop closed so that the square of the lock-in input signal is directly proportional to the work function. The same caveats that were present in the mapping of LDOS apply here as well. The theory above assumes a constant density of states so that the tunneling current is only proportional to the tip-sample distance which is not true for all samples. Since the tunneling current is included in the equation for Φ , opening the feedback loop like is done in dI/dV_b mapping will not help. The signal will always be a convolution of the local work function, LDOS and topography. Nevertheless the square of the dI/dz will give at least qualitative map of barrier height variations.

The above derivation of some of the spectroscopic techniques that are possible with an STM highlights the technique's biggest strength and shortcoming: STM can be used to probe a vast spectrum of local properties unattainable by other techniques, but separating the different signals from one another is not trivial and in many cases requires rigorous analysis.

2.3 Non-contact atomic force microscopy

Atomic force microscopy (AFM) is a very similar technique to STM and can be often performed using the same apparatus. The difference is that in AFM, as its name suggests, the tunneling current as a measure of the tip sample distance is replaced by interatomic forces. There are a plethora of different ways to "sense" the atomic forces between the tip and the sample, especially when operated under ambient pressure. Here only the most common method used under UHV and the first one to achieve true atomic resolution will be discussed, i.e. frequency modulation non-contact AFM (nc-AFM).⁶⁸

In nc-AFM, the tip is attached to a cantilever or a tuning fork which is driven to oscillate at its resonance frequency above the surface. When taking the tip close (≈ 1 nm) to the surface its resonance frequency will

shift due to the new potential landscape introduced by the forces between tip and sample. The frequency shift Δf from the unperturbed oscillation is then used as the measure of how far the tip is from the surface, similar to the tunneling current in STM. Usually a phase-locked loop (PLL) is used to adjust the frequency of the driving oscillation to match the new resonance frequency while another feedback loop keeps the amplitude of the oscillation constant by adjusting the amplitude of the actuator. Finally, in order to obtain a topographic image of the surface, a feedback loop adjusts the height of the tip over the sample while keeping Δf constant. As can be seen already from the number of feedback loops, nc-AFM is a more complicated tool compared to STM.

Depending on the surface and tip material, a host of different forces act between the tip and the sample. For a general description, it is sufficient to only consider the van der Waals forces with a repulsive short range term as these are always present irrespective of the material. A common way to model these is the Lennard-Jones (L-J) potential,

$$w(r) = \epsilon \left[\left(\frac{r_0}{r} \right)^{12} - 2 \left(\frac{r_0}{r} \right)^6 \right], \quad (2.18)$$

where the first term is a semi-empirical repulsive potential describing the Pauli repulsion of the overlapping electron clouds and the second term the van der Waals potential.⁶⁹ The prefactor ϵ gives the depth of the potential while r_0 is the equilibrium distance, i.e. the distance corresponding to the potential minimum. Unlike in STM where the macroscopic shape of the tip has little effect on the tunneling current due to its short range, the van der Waals forces attenuate so slowly that the bulk tip must be taken into account to account for all the forces. The Lennard-Jones potential can be integrated analytically for a paraboloidal tip with radius of curvature R over a semi-infinite bulk. The resulting potential is given by

$$w_{tip-bulk}(r) = \pi^2 \epsilon \rho_{tip} \rho_{sample} R \left[\frac{r_0^{12}}{1760 r^7} - \frac{r_0^6}{3r} \right], \quad (2.19)$$

where ρ_{tip} and ρ_{sample} are the atomic densities of the tip and sample. Figure 2.6 shows the potentials plotted for the atom-atom case (eq. 2.18) and for the bulk-tip case (eq. 2.19). There are two obvious qualitative differences in the curves; the vdW forces for the bulk tip attenuate much more slowly than in the atomic case and the potential minimum is pushed closer towards the sample. This means that when the total force on the tip might be attractive at a given distance, the last atom on the tip apex can already be well in the repulsive regime of the force. This should be taken

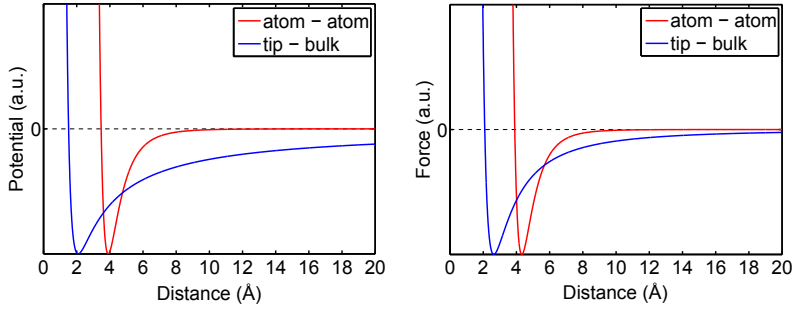


Figure 2.6. Lennard-Jones potential (left) and force (right) for two atoms (red curve) and for a paraboloidal tip over a semi-infinite bulk (blue curve). The depth of the minima of the potentials are scaled to match.

into account when considering the origin of atomic contrast in AFM, even if the repulsive force might not follow exactly the r^{-12} term included in the L-J potential.

In order to understand the relation of the tip-sample forces with the frequency shift measured in AFM it is common to model the tip as a harmonic oscillator in a force field. Assuming a uniform force constant k for the cantilever over the oscillation cycle, the resonance frequency f_0 of the freely oscillating tip is given by

$$f_0 = \frac{1}{2\pi} \sqrt{\frac{k}{m^*}}, \quad (2.20)$$

where m^* is the effective mass of the tip. If the tip is taken close to a surface its resonance frequency will shift due to the new potential landscape introduced by the forces between the tip and sample. By assuming that the derivative of the forces with respect to the oscillation axis $\partial F/\partial z$ is constant over the whole oscillation of the tip, the shift in resonance frequency Δf comes directly from equation 2.20

$$\Delta f = -\frac{f_0}{2\pi k} \frac{\partial F}{\partial z}. \quad (2.21)$$

Depending on the cantilever design in the AFM, the amplitude of the oscillation is typically between $1 \text{ \AA} \dots 20 \text{ \AA}$. Looking at the force-distance curve in figure 2.6, it is clear that the slope of the force is not constant over the oscillation. The varying slope of the force curve can be taken into account in the calculation of the frequency shift by integrating over the oscillation and multiplying the slope at each point of the oscillation by a weight function. The frequency shift is then given by⁷⁰

$$\Delta f(z) = \frac{f_0}{\pi A^2} \int_{-A}^A k_{kt}(z+s) \sqrt{A^2 - s^2} ds, \quad (2.22)$$



Figure 2.7. A scanning electron micrograph of a silicon cantilever used in AFM (left) and a photograph of a qPlus tuning fork (right).

where A is the amplitude of the oscillation and $k_{ts}(z)$ the partial derivative of the force, i.e.

$$k_{ts}(z) = \frac{\partial F}{\partial z}. \quad (2.23)$$

For very large amplitudes the weight function effectively flattens out and the integral in equation 2.22 becomes directly proportional to the force in the midway point of the oscillation, whereas for very small amplitudes it approaches the simple relation given in equation 2.21.

In order to get a large Δf signal from the short range forces, it is beneficial to have the tip very close to the sample, while keeping the oscillation amplitude as small as possible. Traditionally AFM has been done using micro machined cantilevers made of silicon (fig. 2.7) with force constants around $0.1 \dots 40$ N/m and resonance frequencies of $10 \dots 350$ kHz. The problem with such cantilevers is that if taken very close to the sample with a small oscillation amplitude they will snap to contact with the surface when the vdW forces overcome the spring force of the cantilever. In order to solve this problem a new type of force sensor based on a quartz tuning forked was developed in the late 90s.^{71,72} The so-called qPlus sensor is made of a quartz tuning fork, identical to ones used in watches, where one of the beams is glued on to the holder and a thin metal wire is glued on to the end of the other beam (fig. 2.7). The design has several advantages compared to the silicon cantilever: The force constant is much higher (typically around 1800 N/m) allowing very small (< 1 Å) oscillation amplitudes to be used and the resonanance frequency of a quartz tuning fork is not as sensitive to temperature variations as silicon based cantilevers.⁷³ Furthermore the piezoelectric effect of quartz allows for direct electrical measurement of the oscillation compared to the more complicated optical methods usually required with the silicon based cantilevers. Finally, due to the high force constant the same sensor can also be used for regular STM without oscillating the tip.

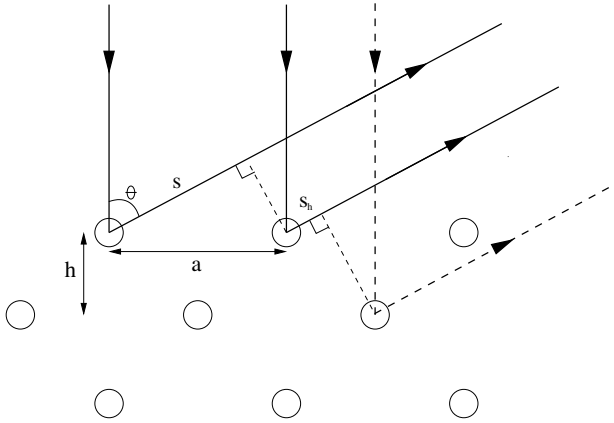


Figure 2.8. 1-D depiction of the Bragg relation (solid lines). The dashed line represents scattering from the second layer of atoms (simple model for IV curves).

2.4 Low-energy electron diffraction (LEED)

2.4.1 Single scattering and the Bragg condition

In addition to the scanning probe methods, low energy electron diffraction (LEED), is one the few ways to study the actual structure of a surface at the atomic level. As the procedure's name suggests, the technique relies on the diffraction of low energy (typically 10...1000 eV) electrons from the surface. The de Broglie wavelength of low-energy electrons is of the same order as typical lattice constants of surfaces. Another benefit in studying surface structures is that the electrons penetrate only a couple of atomic layers into the substrate and hence only probe the very surface of the sample.

The basic process in diffraction can be understood through the Bragg condition (fig. 2.8). When only the surface-most atoms are considered the condition for a diffraction spot can be expressed as

$$\sin \theta = \frac{n\lambda}{a}, \quad (2.24)$$

where θ is the diffraction angle, n the diffraction order and λ the de Broglie wavelength of the electron defined by

$$\lambda = \frac{h}{\sqrt{2mE}}, \quad (2.25)$$

where h is the Planck constant, m the mass of the electron and E its kinetic energy.

Equation 2.24 demands that the path difference (s in fig. 2.8) of electrons diffracted off adjacent surface atoms is a multiple of the electron

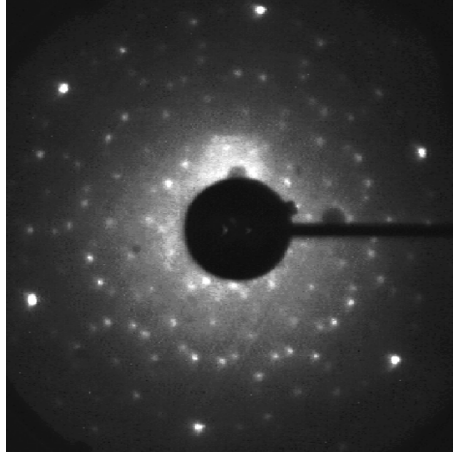


Figure 2.9. LEED pattern of a sulfur $2\sqrt{7} \times 2\sqrt{7}$ -R19.1° adsorbate layer on a silver (111) single crystal. The beam energy used is 55 eV.

wavelength. This condition can be extended for the 2D surface by defining the reciprocal lattice unit vectors⁷⁴

$$\vec{a}^* = \frac{2\pi \vec{b} \times \vec{n}}{A} \quad (2.26a)$$

$$\vec{b}^* = \frac{2\pi \vec{a} \times \vec{n}}{A} \quad (2.26b)$$

and the reciprocal lattice vector

$$\vec{G} = h\vec{a}^* + k\vec{b}^*, \quad (2.27)$$

where \vec{a} and \vec{b} are the real unit vectors, A the area of the surface unit cell defined by \vec{a} and \vec{b} , \vec{n} the unit surface normal vector and h and k integers defining the diffraction order.

Now the diffraction condition (eq. 2.24) can be written as⁷⁴

$$\vec{K} - \vec{K}' = \vec{G}, \quad (2.28)$$

where the \vec{K} and \vec{K}' are the surface parallel components of the wave vectors of the incident and diffracted electrons. Since the incident electron beam in LEED is generally perpendicular to the surface, \vec{K} is zero so that equation 2.28 can be written as

$$-\vec{K}' = \vec{G} \quad (2.29)$$

The LEED pattern essentially presents the surface structure in reciprocal space. The technique is especially useful for studying adsorbate structures or overlayers. Most adsorbate structures will have a larger lattice constant than the substrate, which will show up as extra spots in

the LEED pattern inside the first order substrate spots. Figure 2.9 shows the LEED pattern of a silver (111) single crystal with an adsorbed layer of sulfur forming a $2\sqrt{7} \times 2\sqrt{7} - R19.1^\circ$ structure. The bright outermost spots forming a hexagon are the diffraction spots from the silver surface, while the rest of the spots are formed by two rotationally symmetric domains.

2.4.2 Multiple scattering - Dynamic LEED (LEED-I(V))

The previous calculations allow for all diffraction peaks (different h and k) to be always visible, with the diffraction angle θ changing as a function of the electron wavelength. When scattering from the different atomic planes in the bulk is taken into account this changes. In the 1D model in figure 2.8 the electrons scattered by the second layer (dashed line) must also have the same phase as the electrons that scatter from the surface (solid lines). This causes the diffraction to cancel out in certain directions and the intensity of the diffraction spots as a function of the incident electron energy become peaked at energies given by^{75–77}

$$E = l^2 \frac{h^2}{4m_e a \cos^2(\theta)} - V_{in}, \quad (2.30)$$

where l is the order of diffraction in the out of plane direction, h is the Plank constant, m_e the electron mass, a the sample lattice constant in Å, V_{in} the inner potential felt by electrons in the crystal and θ the direction of scattering given by 2.24. Even though equation 2.30 explains the emergence of peaks in the I(V) curves and their approximate positions, in most cases it falls short of explaining the full spectrum. This can be easily seen in figure 2.10 where the intensities of the two first order diffraction spots, i.e. h and k in eq. 2.28 are either (0 1) or (1 0), of a clean silver (111) surface are plotted against electron energy. Equation 2.30 suggests that the two I-V curves should peak at the same positions and the maxima of the

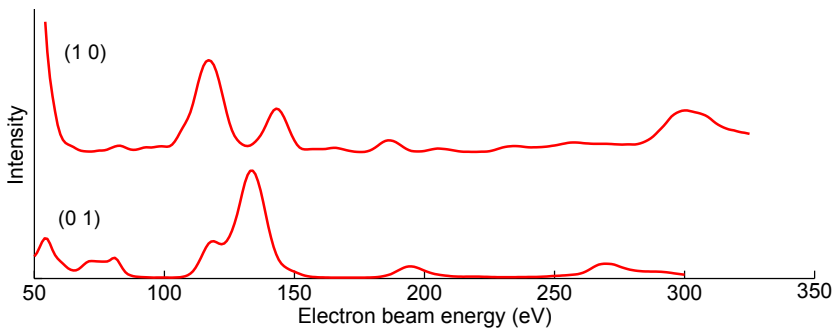


Figure 2.10. LEED I(V) curves measured off the (111) facet of silver.

two curves do roughly coincide, but it is clear that there is fine structure in all the peaks.

In order to fully explain the $I(V)$ curves in electron diffraction, multiple scattering needs to be taken into account, i.e. processes where the electron scatters several times in the crystal before coming out. Although not simple to do, the exact atomic positions of the first few atomic layers of the sample can be deduced from the measured intensities of the various LEED spots as a function of the beam energy. The way this is done is by first guessing a structure for the sample unit cell and then calculating the resulting $I(V)$ curves for the structure and comparing against the measured $I(V)$ curves. The structure is then changed a little and a new set of $I(V)$ curves are calculated. The quality of the match between the calculated and measured $I(V)$ curves is usually done using the so called Pendry R-factor.⁷⁸ As every atom in the unit cell typically has three degrees of freedom, the size of the parameter space to explore to find the correct structure grows rapidly with the size of the unit cell and the method quickly becomes computationally very demanding.

3. Results

In this chapter the main results of the publications included in the thesis are summarized. Apart from Publication IV, all the measurements are done on graphene grown on an iridium single crystal, which has been shown to work as a convenient model system. Publications I and V focus on the study of the structure of graphene on iridium by STM, AFM and LEED. In Publication II, quantum confinement of electronic states in graphene is studied on well-defined graphene quantum dots grown on iridium where the location of each atom is known. Finally in Publications III and IV, the self-assembly of metal-phthalocyanine molecules is studied as a candidate to introduce a well-defined potential modulation on graphene.

3.1 Structure of epitaxial graphene on Ir(111)

As already mentioned, graphene forms a moiré pattern on Ir(111) due to the lattice mismatch between graphene and the metal substrate. Depending on the growth conditions, the unit cell of the moiré can either be commensurate or incommensurate, with the period of the moiré in the different phases being around 10×10 graphene rings over 9×9 iridium atoms.⁷⁹ The slight variations arise from the fact that at room temperature, the graphene sheet is under strain due to the difference in the coefficients of thermal expansion between graphene and iridium.^{79–81} The different areas of the moiré have been named according to the stacking of the center of the benzene rings and are illustrated in figure 3.1. Typically on epitaxial graphene on metals exhibiting a moiré pattern, the graphene-substrate distance is largest around the top sites of the moiré.^{31,46} The interaction with the metal is strongest on the hcp and fcc sites where one of the graphene sublattices sits directly on the top of a metal atom and

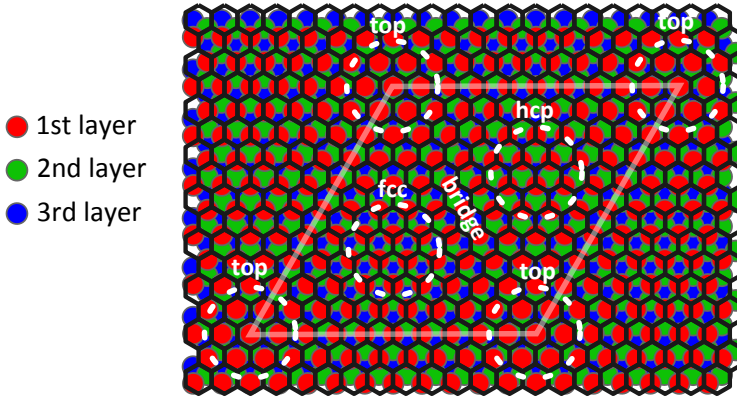


Figure 3.1. Schematic figure of the naming of the different areas of the moiré for graphene on the (111) facet of an fcc crystal.

hence also the graphene-metal distance is decreased.

The moiré pattern is easily visible in STM images where the contrast of the moiré changes with the sample bias.⁵⁸ Typically with a low sample bias the moiré contrast is inverted and the top sites are imaged as depressions rather than protrusions.⁵⁸ The contrast of the moiré is inverted around $-1.5 \text{ V} \dots 0.5 \text{ V}$,⁸² but the exact tip termination may also change the contrast irrespective of the bias.⁵⁸ In fact, it is not only the electronic states and topography which are modulated over the moiré, but also chemical reactivity.⁸³ This makes the study of the structure with local probes challenging as the image is always a sum of several signals which cannot be easily deconvoluted.

The large unit cell and incommensurability on the other hand make the computational study of the system by density functional theory (DFT) difficult. It also seems that the epitaxial graphene systems are very sensitive to the exact exchange correlation functional used in the calculations.⁸⁴ Furthermore the interaction in the weakly interacting systems, such as graphene on iridium, are dominated by non-local van der Waals forces which are in general difficult to model by DFT.^{85,86}

In Publication I, we have studied the topographic structure of the graphene moiré by simultaneous AFM and STM using a qPlus sensor. We observed the same contrast inversion in STM as had been reported in literature (fig. 3.2a and b). There is also clear contrast in the dI/dV_b and dI/dz signals over the moiré, measured at constant current. The problem in interpreting these is that by having the feedback loop closed, the tip-sample distance most likely changes over the moiré which will affect the measured signal. On the other hand, no direct information can be

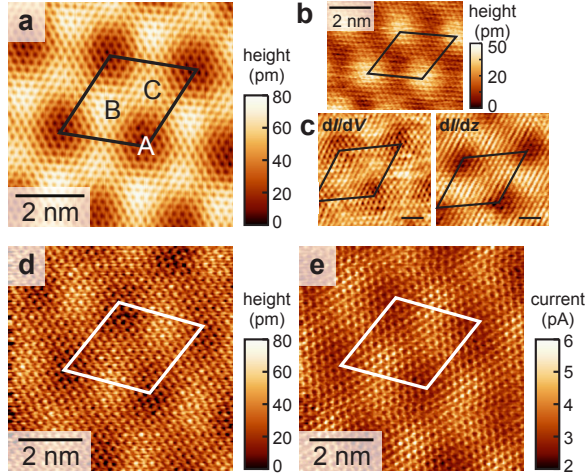


Figure 3.2. (a) Constant-current STM topography image of epitaxial graphene on Ir(111) acquired at $V_b = 0.3$ V and set-point current of 0.3 nA. The line indicates the moiré unit cell and the three inequivalent areas within it are denoted by A, B and C. (b) High-bias STM image, taken at 0.45 V / 1 nA, showing the inverted moiré pattern. (c) Constant-current dI/dV_b and dI/dz maps recorded at a bias of 0.05 V. (d) Constant frequency shift AFM image with $\Delta = -45$ Hz and $V_b = 0.01$ V. (e) Average current over the tip oscillation cycle measured simultaneously under AFM feedback.

extracted from constant height scan either as the surface is corrugated. The surprising result in Publication I is that the constant frequency shift AFM image (fig. 3.2d) looks similar to the low bias STM images with depression on a higher background rather than protrusions as one would expect from DFT and other similar systems. The depressions in AFM can be correlated to the same position with the depressions observed in STM by switching back and forth with the AFM and STM feedbacks.

It turns out that the tip in the AFM measurement oscillates so close to the graphene that the varying chemical forces, also responsible for the preferred nucleation sites of metal nanoclusters,⁴¹ induce a false contrast in the AFM measurement. A systematic measurement of the contrast inversion in AFM with metal tips was later performed by two separate groups,^{82,87,88} where the false contrast was reproduced and explained in quantitative fashion.⁸⁸

In order to eliminate the variation in the chemical reactivity, the metal AFM tip can be passivated by terminating the end of the tip with something that does not like to form bonds with the surface. Picking up an individual carbon monoxide molecule on the apex of the tip has become a well-established method to passivate the tip when imaging individual molecules on surfaces.^{89–93} The carbon on the CO adsorbs on the metal

tip and the oxygen is left sticking out perpendicular to surface, which, in addition to passivating the tip, conveniently makes the tip apex atomically sharp.^{94–96}

In Publication V, we have used a CO terminated tip to study the moiré pattern with AFM. The Δf setpoint in the AFM scans was chosen on the repulsive branch of the $\Delta f - z$ curve. Since the CO does not bond to the graphene, the main force we are probing is the Pauli repulsion between the electron clouds on the CO and the sample. As can be seen in figure 3.3 the AFM image with the CO tip produces the same moiré contrast as predicted by DFT,⁸³ i.e. protrusions on the top sites and graphene closer to the iridium substrate near the hcp and fcc sites. By looking at the structure in more detail, even the slight height difference between the hcp and fcc sites is reproduced in the scan (fig. 3.3b).

To further corroborate on the structure of the moiré we also performed a LEED-I(V) measurement of a full monolayer of graphene grown on iridium. Traditionally dynamic LEED has been used to obtain the adsorption sites of individual atoms on metal single crystals which exhibit much smaller unit cells compared to the graphene moiré on iridium. For the LEED model of the graphene moiré, we used a commensurate structure of 10×10 carbon rings over 9×9 iridium atoms. Along with the graphene, the top three iridium layers were relaxed in the modeling. In total this comprises 200 carbon atoms and 243 iridium atoms. The structure was first allowed to relax without any restrictions, but this did not yield a satisfactory end result as the number of free parameters was just too high ($443 \text{ atoms} \times 3 \text{ degrees of freedom}$). Since the variation in the graphene layer is rather smooth its structure could be presented using low order Fourier components. A similar scheme had been shown to work in a LEED-I(V) study of graphene grown on ruthenium.⁹⁷

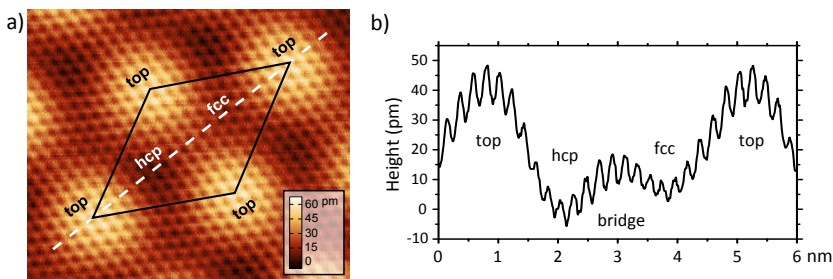


Figure 3.3. (a) Constant frequency shift AFM image of the graphene moiré ($\Delta f = 0 \text{ Hz}$, bias = 0 V). (b) AFM line profile over the moiré unit cell marked with a white dashed line in (a).

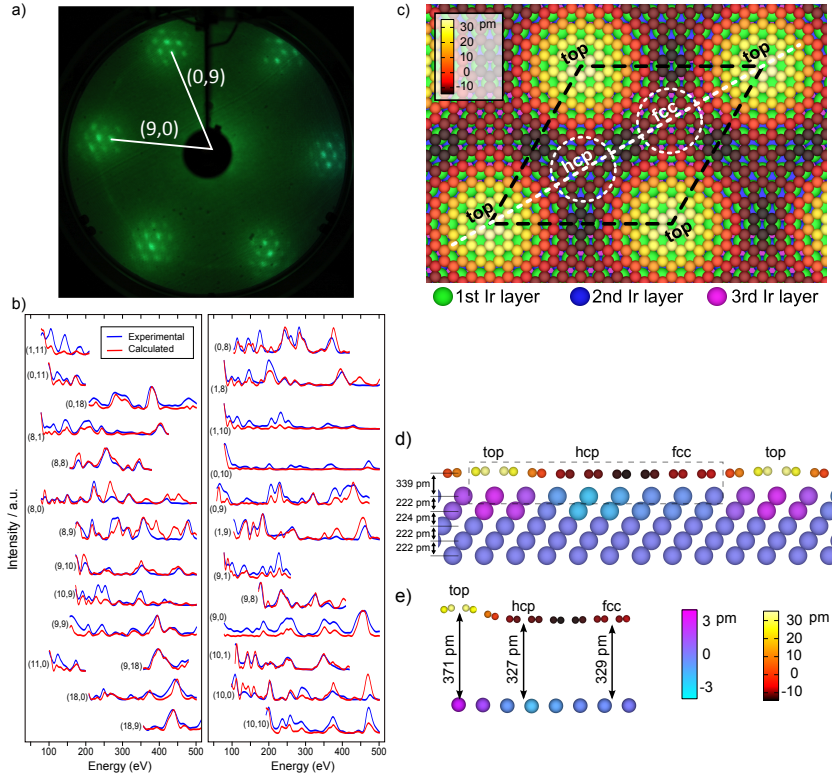


Figure 3.4. (a) LEED pattern of graphene on iridium (78 eV) showing the moiré spots. The illustrated indexed spots correspond to the first order substrate spots. (b) Comparison of the experimentally measured (blue) and calculated (red) I(V)-curves for the best fit (7886 eV, $R_P = 0.39$). (c) The topographic structure of the moiré unit cell obtained from LEED-I(V). (d) Cross section through the moiré unit cell of the LEED-I(V) model along the white dashed line marked in (c). The color scales of the z-positions of the atoms are relative to the mean height of the layer, given on the left side of the image. (e) Magnification of the area marked with the dashed box in (d). The vertical scale in (e) is magnified 5-fold to better illustrate the shape of the graphene layer.

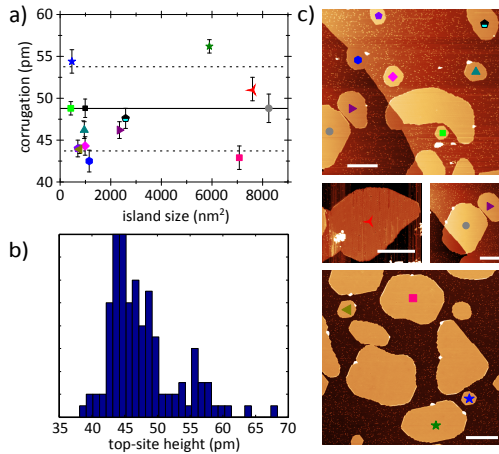


Figure 3.5. (a) The moiré corrugation as a function of graphene island size excluding the outliers. The solid line is the average of the set and the dotted lines the standard deviation. (b) Distribution of all the individual top site heights extracted from the AFM images (including outliers). (c) Overview STM scans of the islands in the plot in (a). The scale bar is 50 nm in all images

The resulting structure from the LEED-I(V) analysis is shown in figure 3.4. The structure is qualitatively similar to that obtained by AFM and DFT. The nice feature of LEED-I(V) is that it gives the atomic positions of the whole unit cell including the subsurface atoms, i.e. iridium in this case. This allows one to obtain the adsorption heights in addition to the surface corrugation. Apart from the top site, the adsorption heights match the DFT results very well. The same trend appears in both of our experimental measurements for the moiré structure: the corrugation of the moiré is markedly larger in the experimental measurement compared to the DFT result. Similar results had also been obtained by X-ray standing waves (XSW) where the corrugation of the moiré from the XSW measurement was significantly larger than that of the DFT calculation.⁸³ The XSW measurements also indicated that the corrugation would be coverage dependant.^{83,98}

To study if the size of the graphene flakes is correlated with the moiré corrugation, we used AFM with a CO terminated tip to image several graphene islands of different sizes. Interestingly, the corrugation of the moiré varied substantially from island to island, but with no correlation on the islands size (fig. 3.5). Furthermore the corrugation of the moiré was not constant even over a single island but exhibited both a smooth variation and individual outliers where the top site was roughly 10 pm higher than on average (fig. 3.6).

The exact cause of the non-uniform corrugation is unclear, but it is most

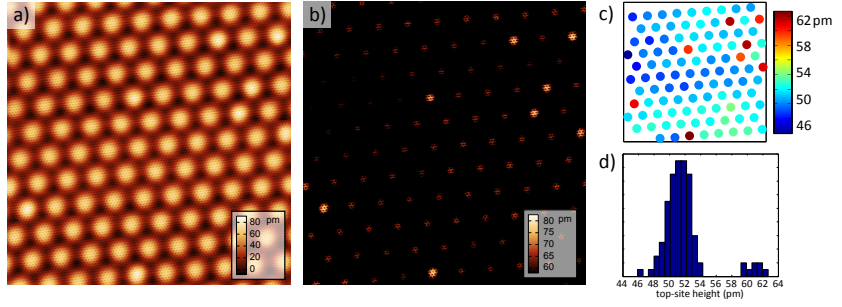


Figure 3.6. (a) Constant frequency shift AFM image over a larger area ($\Delta f = 0$ Hz, bias = 0 V, 24×24 nm²). (b) Same AFM image as in (a) but with the contrast adjusted to the top sites. (c) Heights of the top sites with respect to the neighboring hcp sites. (d) Distribution of the top site heights in (c)

likely related to the incommensurate moiré and the strain in the graphene lattice after cooling. As the structure is incommensurate, the exact adsorption registries of the top sites (or hcp or fcc sites) are different. This could influence the interaction between the substrate and graphene, leading to the observed slowly varying corrugation, similar to a second order moiré. As graphene on iridium can be locally sheared,⁸⁰ a second order moiré would not necessarily produce an ordered pattern. In larger graphene islands, the strain in the graphene layer at room temperature is partly relieved by local delimitation into wrinkles. The islands we studied showed no wrinkling, most likely due to their small size. The observed outliers could however be a way to relieve some of the strain before complete delamination into a wrinkle.

3.2 Confined electronic states in graphene

As has already been shown, graphene can be grown into very small and well-defined islands on iridium. Based on angle resolved photoelectron spectroscopy (ARPES), the occupied side of the graphene Dirac cone is also known to survive on iridium. These qualities make graphene on Ir(111) a very nice model system to study quantum confinement in graphene. In Publication II we have studied the electronic states confined in several small graphene islands and by the help of computational modeling extracted the dispersion relation in the structures.

Figure 3.7a shows an STM image of a typical area of iridium surface with graphene islands after TPG growth at 1470 K. Most of the larger structures are agglomerates of several graphene islands with grain bound-

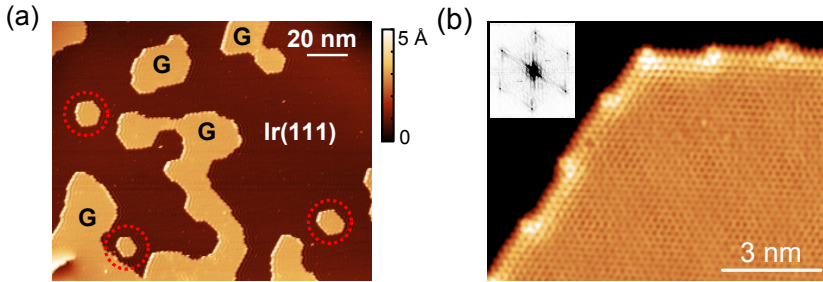


Figure 3.7. (a) Large-scale STM image of graphene islands (G) on an Ir(111) substrate (acquired at $I = 40$ pA and $V_b = 1.0$ V). Small graphene QDs have been indicated by red circles. Atomic resolution STM image (50 mV / 200 pA) of a graphene flake edge where the zigzag termination of the edge and the kinks of one atomic row are clearly visible. The inset shows the FFT spectrum of the image.

aries running through them. The smaller isolated islands marked with the red circles on the other hand are defect free. As can be seen from the closeup STM image on one of the graphene islands in figure 3.7b the edges are all terminated in the zigzag direction of the graphene lattice with steps of single atomic rows at intervals of the moiré pattern.

Figure 3.8a shows a perfectly symmetric small graphene island with just seven carbon rings on each edge. Measuring dI/dV_b spectra on different part of the island gives two distinct spectra with peaks at different energies (fig. 3.8b). By mapping the differential conductance over the graphene flake at the energies of the peaks we can visualize the LDOS of the corresponding states over the island (fig 3.8c). Both states resemble eigenstates of a particle in a box problem; the lower energy state with 1S symmetry shows no nodes, whereas the higher energy state can be reproduced from two degenerate 1P type waves (fig. 3.8d).

Similar states are found also in other graphene islands or quantum dots (GQD), with the energy of the states scaling with the island size as one would expect. We can model the states by tight-binding calculations, as we can extract the exact atomic positions, or by continuum wave-equation with linear dispersion. The correct equation for graphene would be the Dirac equation for massless particles presented in Chapter 1. However the boundary conditions for the Dirac equation are non trivial and solving it numerically for the GQD geometries becomes difficult.⁹⁹ Here we use the Klein-Gordon (KG) equation¹⁰⁰

$$-v_F^2 \hbar^2 \nabla^2 \psi_i = E_i^2 \psi_i, \quad (3.1)$$

where v_F is the Fermi velocity. The KG equation actually describes rela-

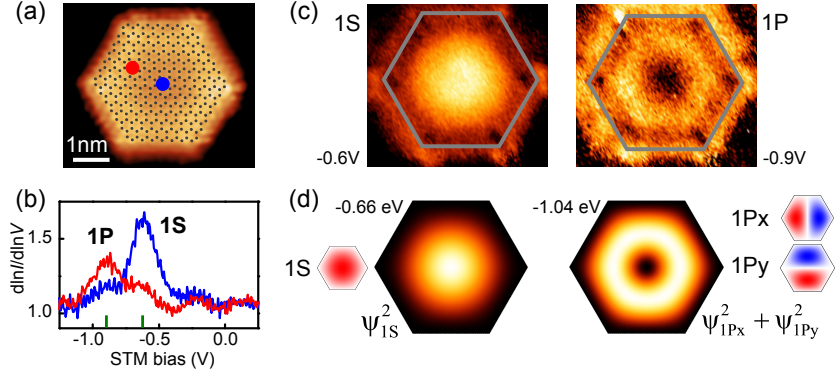


Figure 3.8. (a) STM topography of a small GQD (-0.05 V and 100 pA) with an overlaid atomic model. The GQD has perfect hexagonal symmetry with 7 benzene ring long edges. (b) Normalized differential conductance spectra measured on the points indicated in (c), the green bars indicate the bias voltages corresponding to the LDOS maps shown in (c). (c) Measured LDOS maps (gray line denotes the edges of the GQD) at bias voltages corresponding to the two resonances in the spectra shown in (b). (d) The corresponding LDOS maps calculated for a particle in a box at the indicated energies and the underlying eigenstates.

tivistic spinless particles, but its use here can be motivated by comparing it to the Dirac equation in an infinite system. The two components of the Dirac equation can be written separately as

$$\begin{aligned} -iv_F\hbar(\partial_x - i\partial_y)\psi_b &= E\psi_a \\ -iv_F\hbar(\partial_x + i\partial_y)\psi_a &= E\psi_b \end{aligned} \quad (3.2)$$

Separating the components gives the Klein-Gordon equation for both sublattices

$$\begin{aligned} -v_F^2\hbar^2\nabla^2\psi_a &= E^2\psi_a \\ -v_F^2\hbar^2\nabla^2\psi_b &= E^2\psi_b \end{aligned} \quad (3.3)$$

For an infinite graphene flake (i.e. ignoring the effect of boundary conditions), all the solutions of the Dirac equation are also solutions of the Klein-Gordon equation.

The boundary condition we use for the GQD edges is given by $\psi_i = 0$. Hence the KG equation will not reproduce edge states, which come out from the coupling of the imaginary parts of the two eigenstates on the edge in the Dirac equation.⁹⁹ As we are only modeling the delocalized states inside the graphene island this should not be a problem. Since the energy of the eigenstates E_i of the KG equation scales linearly with v_F , we can obtain the Fermi velocity in the quantum dots directly from the slope when plotting the bias of the dI/dV_b maps against the energy of the corresponding KG state.

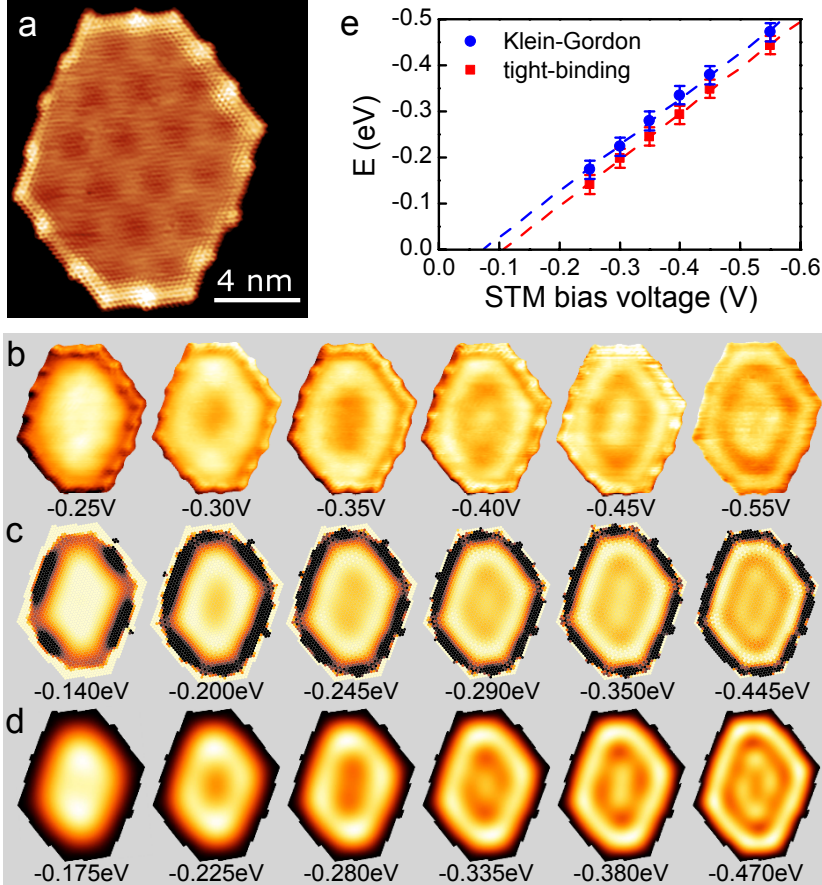


Figure 3.9. Detailed comparison between STS experiments and computational results on a large GQD. (a) Atomically resolved STM image of the GQD ($I = 3$ nA, $V_b = 1$ mV). (b) dI/dV_b maps recorded under constant-current STM feedback at the bias voltages indicated in the figure ($I = 1$ nA). (c),(d) Corresponding LDOS plots at the indicated energies calculated using a TB model (c) and the KG equation (d) as described in the text. (e) Correspondence between the experimental and the calculated energies based on TB (red squares) and the KG equation (blue circles) calculated with $v_F = 6.2 \times 10^5$ m/s.

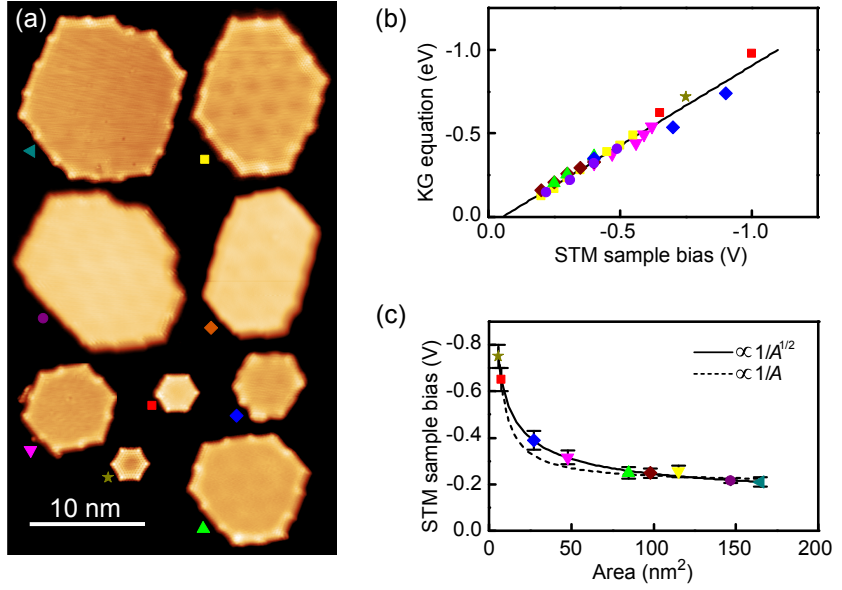


Figure 3.10. Electronic structure of GQDs as a function of their size. (a) STM topographies of the GQDs used for the plots in panels (b) and (c). (b) The correspondence between the energies derived from the STM experiments (x -axis) and those calculated from the Klein-Gordon equation using a single value for v_F (y -axis). (c) STM sample bias corresponding to the S state as a function of the area A of the GQD. The solid and dashed lines are fits to $1/\sqrt{A}$ and $1/A$ scaling, respectively.

The KG equation was solved for the various geometries of the GQDs by first extracting the dimension of the GQD from the STM image and then solving the KG equation numerically for the exact shape using the finite element method. For the larger asymmetric islands the KG equation has several almost degenerate solutions. The measured dI/dV_b maps were hence compared to composite maps generated from the KG eigenstates ψ_i by gaussian broadening. The LDOS map at a certain energy E is then given by

$$LDOS(E, x, y) = \sum_i \left[e^{-\frac{(E-E_i)^2}{2\sigma^2}} \psi(x, y)_i^2 \right] \quad (3.4)$$

The energies of the LDOS maps were then visually matched with the measured STS maps. Figure 3.9b shows a set of STS maps measured from a large GQD (3.9a) along with simulated maps calculated by TB (3.9c) and the KG equation (3.9d). The TB eigenstates were broadened equivalently to the KG eigenstates. Both TB and the KG equation reproduce the measured maps well giving roughly the same value of $v_F = 6.2 \times 10^5$ m/s for the Fermi velocity, which is comparable although slightly smaller than values reported from ARPES measurements for a full monolayer of graphene on Ir(111).^{27, 53, 101}

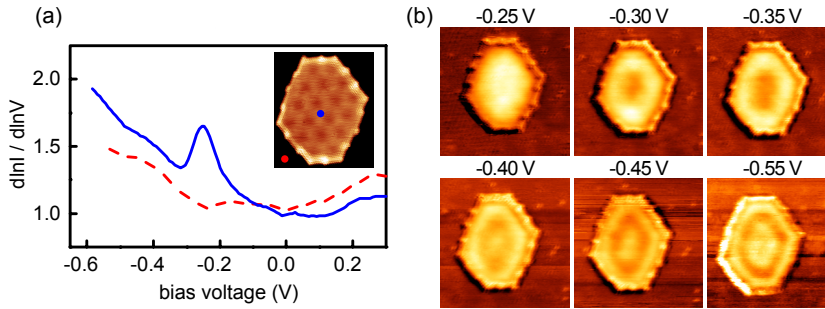


Figure 3.11. (a) $d\ln I/d\ln V_b$ spectra measured in the middle of the GQD shown in the inset (blue solid line) and on top of the Ir(111) substrate (red dashed line). This is the same GQD as shown in figure 3.9 (b) Experimental dI/dV_b maps from figure 3.9 at the biases indicated in the figure showing the background, i.e. the surrounding Ir(111) substrate. Set-point current 1 nA.

To study if the Fermi velocity is constant across different GQDs, we mapped the LDOS of 9 graphene islands of different sizes and shapes shown in fig. 3.10a and compared them to simulated maps using the KG equation. The states could be fit on the line presented in figure 3.10b using a single value for v_F , verifying that the Fermi velocity does not change from one island to the next. To further corroborate that the states follow a linear dispersion we have plotted the S state as function of the area of the GQD in figure 3.10c. For massive particles obeying the Schrödinger equation, the energy (V_b) of the states should scale as $1/A$, whereas for relativistic massless particles the energy of the states scale as $1/\sqrt{A}$. It is clear from figure 3.10c that the $1/\sqrt{A}$ is a better fit to the energy scaling of the states.

Around the time of the publishing of Publication II, three other papers dealing with the same system came out. The first two publications largely agree with our conclusions even if their modeling of the states is slightly different from ours.^{102,103} The last paper however attributes the observed states to a locally gated iridium surface resonance.¹⁰⁴ The onset of the Ir(111) surface resonance has been shown to shift under graphene roughly to the energies where we see the lowest eigenstates (~ -0.2 eV).¹⁰⁵ The clear difference to our measurements is that we rarely see a large onset of the surface resonance on the bare iridium, whereas in the paper by Altenburg et al.,¹⁰⁴ the intensity of the dI/dV_b signal is much higher on the adjacent iridium from -0.4 V onwards. Figure 3.11 shows the same quantum dot as in figure 3.9, but with the adjacent iridium included. As can be seen, there is no strong onset of the Ir surface resonance even at a bias of -0.55 V where the state should already be present. Furthermore our measure-

ments seem to fit the model with linear dispersion very well, although the sampling might be from such a small area that it would be difficult to detect the curvature in the parabolic dispersion. It is in any case very difficult to tell the states apart, as the slope of the surface resonance in the band structure is very similar to that of the Dirac cone in graphene on Ir(111).¹⁰⁵

The reason behind the seeming discrepancy in the measurements might arise from the exact tip termination, where one tip is more sensitive to the states at the K-points of the Brillouin zone, while others mainly probe the center of the Brillouin zone, i.e. the Γ point. In this case the where there are no states near the Fermi level in graphene. A similar situation is present on graphene transferred on to an insulator, where one group observes a gap near zero bias in several of their graphene dI/dV_b spectra,¹⁰⁶ while other groups do not see the same effect in the same sample. The gap is explained through the conservation of momentum of the tunneling electron. As the states near the Fermi-level in graphene all reside at the Dirac points, i.e. states with momentum in the graphene plane, the tunneling electron with no momentum in the graphene must excite a phonon in graphene to acquire the in-plane momentum corresponding to the K (or K') point.¹⁰⁶

3.3 Molecular self-assembly on graphene

Self-assembly of ordered molecular layers on graphene has gained interest in the scientific community as a means of influencing the graphene band structure. On the one hand, an ordered weakly interacting molecular layer can be used to shift the Fermi level in a uniform manner, in contrast to substitutional doping, where the doping is not uniformly distributed over the graphene layer.¹⁰⁷ On the other hand it has been proposed that a periodic potential modulation can be used to reshape the Dirac cones of graphene.^{27,28} It is even possible to envision a molecular lattice whose adsorption is such that it breaks the sublattice symmetry in graphene, consequently opening a band gap at the Dirac points.

Adsorption of organic molecules on highly ordered pyrolytic graphite (HOPG) has been extensively studied in literature.^{108,109} Even though the top layer of HOPG is essentially graphene, the adsorption of molecules on actual graphene devices will be affected by the roughness induced by the substrates on the graphene. Silicon dioxide, the typical substrate used in

graphene devices, has a significantly higher roughness compare to HOPG. In contrast, on atomically smooth hexagonal boron nitride, the top performer as a graphene support, graphene produces a moiré pattern.¹¹⁰

In Publications III and IV, we have studied the self-assembly of cobalt phthalocyanine (CoPc) first on epitaxial graphene on Ir(111) and then on transferred graphene on. Phthalocyanines (Pc) form a series of commercially available molecules that consist of a metal center (Zn, Fe, Mn, Co, Cu, Ni, etc.) surrounded by an organic macrocycle. The strength of the interaction between graphene and Pcs can be tuned by going from one metal-Pc to another. Hence they make for a versatile model template for studying molecule-graphene interactions.

Graphene on Ir(111) offers a nice model system to study the adsorption of CoPc (3.12a) as graphene can be grown over the whole surface in a single orientation. This allows one to use electron diffraction to study the long range order of the self assembled layer, which is not possible on transferred graphene samples. Upon adsorption on graphene/Ir(111), CoPc forms a roughly square lattice shown in the STM scan in figure 3.12b. The CoPc domains extend over terraces and are typically only interrupted at the iridium step edges.

The LEED pattern (fig. 3.12c) from the structure shows a large number of diffraction spots at low energies. This is to be expected of an lattice with rectangular symmetry over a hexagonally symmetric substrate as several equivalent rotational domains will always exist. The STM image in figure 3.12b has been obtained with a bias voltage above the lowest unoccupied molecular orbital (LUMO). Hence the tunneling is mediated through the molecular orbital and the structure of the molecule is not visible. By scanning with a bias voltage below the LUMO and above the

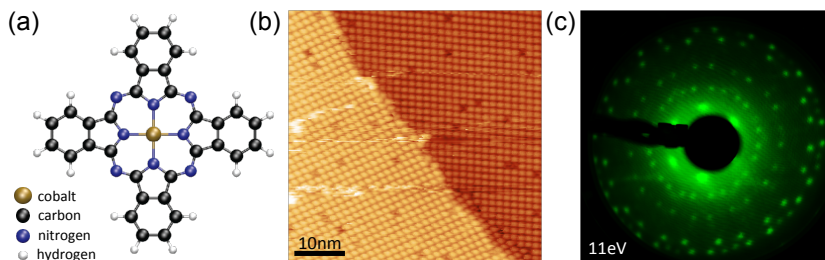


Figure 3.12. (a) Schematic figure of the structure of the CoPc molecule. (b) STM image (4 pA / 0.66 V) of the surface after the deposition of a monolayer of CoPc. (c) LEED pattern after CoPc deposition. The hexagonal pattern in the center is the first order spots of the graphene moiré pattern while the rest of the spots arise from the molecular lattice.

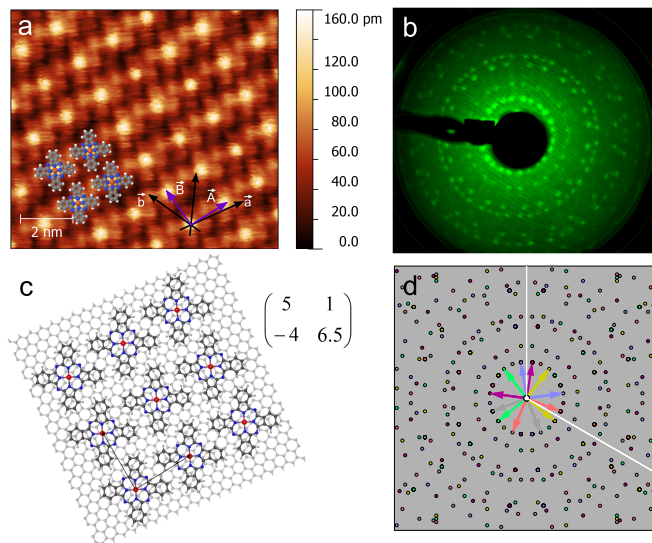


Figure 3.13. Proposed adsorption structure from STM images and LEED. a) In gap STM image revealing the molecule backbone (-130 mV / 2.5 pA). The unit cell of the CoPc adlayer is marked with vectors \vec{A} and \vec{B} while \vec{a} and \vec{b} denote the directions of the graphene lattice vectors. b) LEED pattern measured from the corresponding structure (27 eV). c) Proposed structure from STM images and LEED patterns. d) Simulated LEED pattern from the proposed structure. The different colors correspond to different rotational domains and the white lines denote the substrate lattice symmetry.

highest occupied molecular orbital (HOMO), the molecule backbone becomes visible and the exact orientation of the adsorbed molecule can be extracted. An STM image taken in-gap, i.e. with a bias voltage between the frontier molecular orbitals, is shown in figure 3.13a which allows one to visualize the packing of the molecules. The LEED pattern of the CoPc layer (fig. 3.13b) can be reproduced by the nearly square lattice shown in figure 3.13c which produces the diffraction pattern shown in figure 3.13d. The angle between the two lattice vectors of the molecule layer is 88.6° . The molecule lattice demonstrates the sensitivity of the LEED pattern to even the slightest changes in the diffracting layer; trying to force the angle to 90° would produce a significantly different looking pattern.

The nearly square packing is common for Pcs and has been also observed on HOPG¹¹¹ and metals substrates.^{112,113} The square packing is most likely governed by molecule-molecule interactions rather than molecule-graphene interactions as the hexagonal symmetry of the graphene nor the moiré is translated to the molecule layer. This is in contrast to the adsorption of FePc on graphene grown on Ru(0001), where the graphene moiré guides the structure of the molecule layer forming a Kagome lattice.¹¹⁴

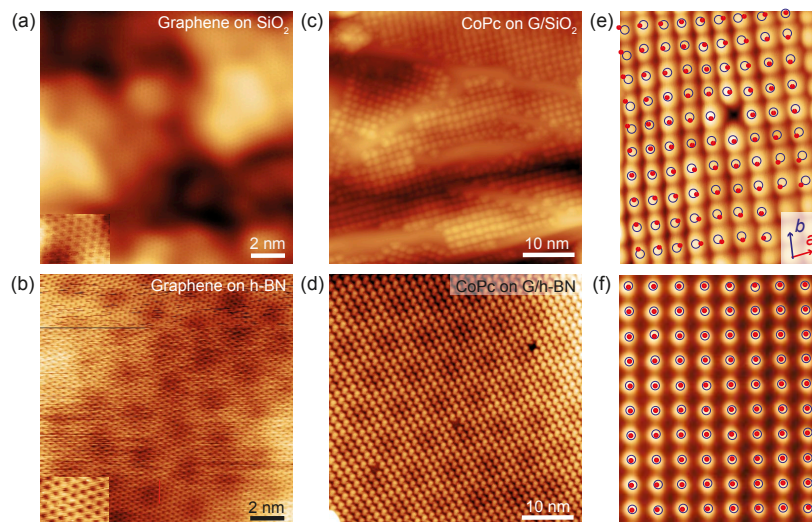


Figure 3.14. Overview STM scans on G/SiO₂ (a, set-point 0.2 V/170 pA) and G/h-BN (b, set-point 0.68 V/40 pA) before the deposition of molecules. The insets show zoomed in images of the graphene atomic lattice. (c,d) Overview STM scans on CoPc molecular layers on G/ SiO₂ (c, set-point 0.71 V/5 pA) and G/h-BN (d, set-point 1.40 V/5 pA). (e,f) STM images of a single domain of CoPc molecules on (e) G/SiO₂ and (f) G/h-BN where the centers of the molecules are marked with blue circles and compared with a rectangular lattice marked with red circles.

Even though the moiré symmetry does not appear in the CoPc layer, there is still some molecule-substrate interaction, since the principal axis of the self-assembled layer has preferred orientations with respect to the underlying graphene lattice, as can be seen from the LEED results.

In Publication IV, we studied how the self-assembly of the CoPc molecules is affected by the roughness of more realistic graphene substrates, SiO₂ and h-BN in this case. The graphene was grown on a copper foil in a separate tube reactor and then transferred on to a thermally oxidized silicon chip with exfoliated flakes of h-BN on top. The graphene covered an area spanning over several h-BN flakes and the SiO₂ in between them. Hence the same sample could be used to study the self-assembly on both SiO₂ and h-BN.

Due to its flexibility, graphene conforms to the shape of the underlying substrate. Figures 3.14a and b show STM images of graphene on SiO₂ and h-BN, respectively. It is clear that the SiO₂ is much rougher compared to the graphene on h-BN. The faint long-range hexagonal pattern seen on the graphene on h-BN is the moiré pattern between the graphene and h-BN lattices. Upon adsorption of the CoPc molecules, the effect of the surface roughness becomes evident: On graphene on SiO₂, the domain

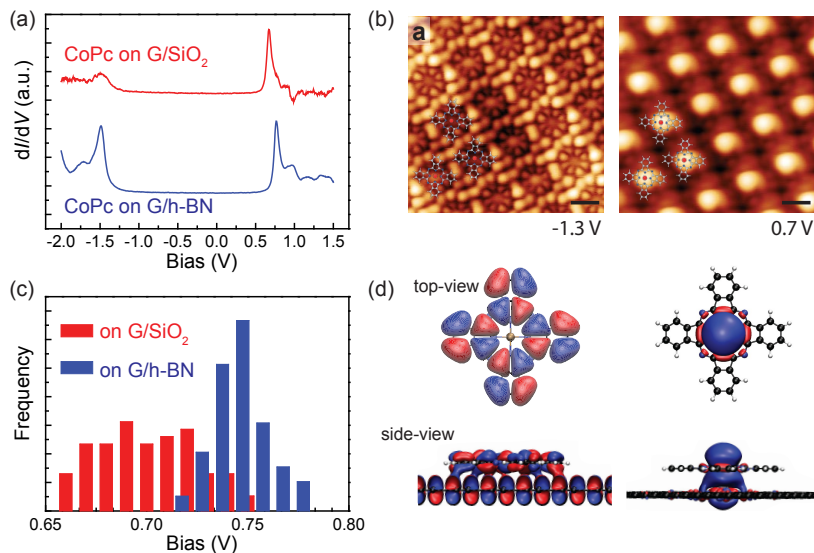


Figure 3.15. (a) dI/dV spectra measured in the middle of a CoPc molecule on G/SiO₂ and G/h-BN substrates. (c) Distribution of the energy of the LUMO on the different substrates. (d) The CoPc frontier molecular orbitals on graphene calculated from DFT using the PBE functional.

size of the CoPc islands is restricted by the roughness of the surface (fig. 3.14c) while on graphene on h-BN the molecules behave like on graphene on Ir(111) forming extensive islands with a similar square lattice (fig. 3.14d). It is not possible to measure LEED on the transferred samples as the size of the h-BN flakes is much smaller than the electron beam size. Nevertheless, by comparing the graphene lattice next to a molecule island to the lattice of the molecules, it would seem that the same adsorption orientation prevails on the G/h-BN as did on the G/Ir(111).

By looking at the molecular lattice in more detail, it becomes clear that there is further disorder inside the CoPc islands formed on the G/SiO₂. Figures 3.14e and f show close up STM images of the CoPcs on SiO₂ and h-BN. The overlaid blue circles represent the centers of the molecules while the red dots on top are a rectangular grid which has been optimized to fit on top of the molecule centers by a least squares fitting. For the molecules on G/h-BN in figure 3.14e the dots sit nicely inside the circles whereas the same cannot be said for the molecules on G/SiO₂ where the correlation between the dots and circles is much worse.

Figure 3.15a shows differential conductance (dI/dV_b) spectra measured on CoPc on G/h-BN and G/SiO₂. Figure 3.15b shows the shape of the frontier molecular orbitals. By measuring dI/dV_b spectra over several molecules it turns out that the disorder in the CoPc lattice is translated

also to variations in the energies of its frontier molecular orbitals. The spread of the LUMOs is shown in the histograms in figure 3.15c. The variation in the position of the LUMO of the CoPcs adsorbed on G/SiO₂ is clearly larger of the two. The reason is most likely not only in the ordering but also in the charge distribution in graphene. The Dirac point with respect to the Fermi level has been shown to vary much more on SiO₂ than on h-BN.^{110, 115–117} On the other hand moiré patterns of epitaxial graphene have been shown to shift molecular resonances, which could be the source of the slight variation observed on graphene on h-BN.¹¹⁸

4. Summary and outlook

In this thesis, possible ways for the modification of the graphene band structure were explored. Most of the measurements were done on the model system of epitaxial graphene grown on iridium(111), and Publications I and V focus on understanding its structure. Determination of the geometric surface structure down to the atomic level is crucial in understanding of the correlation between electronic and geometric structure of surfaces. This is an extremely topical problem with the rise of two-dimensional materials on solid supports (e.g. graphene, hexagonal boron nitride, silicene etc.). Structure determination on this type of materials is notably difficult as they typically have large unit cells and locally varying density of states and chemical reactivity. Publication V presents the first experiments to give the positions of the carbon atoms in epitaxial graphene on Ir(111). The average structure and graphene-iridium distances on different areas of the moiré are extracted from the LEED-I(V) analysis while the AFM experiments with a CO modified tip show that the corrugation of the moiré pattern varies. The variations of the moiré are most likely a result of the various possible adsorption phases present in the system.

In Publication II, we use STM to map quantum confined states in graphene nanostructures. We show that the spacing of the states matches with that assumed from linear dispersion. The Fermi velocity in the small structures also matches the value measured for full coverage of graphene very well. A simple continuum approach to model the states using the Klein-Gordon equation is presented and validated by comparing to the STS maps and TB calculations. There are many theoretical proposals on the new types of electrical devices that could be constructed if atomically well-defined graphene nanostructures were available. Top-down lithography is currently not sufficiently precise for this purpose and bottom-up

approaches are being developed. For example, the graphene quantum dots grown on Ir(111) could form a starting point of this process. However, methods to passivate and stabilize the graphene zigzag edges need to be developed along with a way of either decoupling the graphene from the metallic substrate, or of transferring them onto the desired insulating substrate.

Another aspect of the work described in Publication 2 is that there are conflicting reports in the literature on STM spectroscopy experiments on both this type of graphene nanostructures as well as bulk graphene samples. This discrepancy is likely to be caused by the differences in the tunnelling coupling between the STM tip and the graphene. They highlight the need to better understand tunneling into two-dimensional structures as they are becoming ever more prominent within the scientific community. So far, tunneling in STM has mainly been considered from the basis of the LDOS and the overlapping of the tip and sample orbitals, while restrictions on the momentum of the electron states have been largely omitted.

In Publications III and IV, the self-assembly of metal phthalocyanines is studied on graphene on different substrates. The self-assembly of the molecules is shown to depend heavily on the roughness of the graphene substrate. On silicon oxide the molecules order only very locally while on graphene on Ir(111) or h-BN, they form extensive islands with a single orientation. Hence if self-assembled molecular layers were to be used to alter the graphene band structure the devices would need to be built on an atomically smooth substrate such as h-BN. It is difficult to assess the effect of the molecules on the graphene band structure by STS measurements. This will be studied in the future by transport measurements, which should allow determining the doping of the graphene by the molecules as well as evaluating the possible changes in the graphene band structure.

Bibliography

- [1] H. W. Kroto, J. R. Heath, S. C. O'Brien, R. F. Curl, and R. E. Smalley, "C60: Buckminsterfullerene," *Nature*, vol. 318, pp. 162–163, 11 1985.
- [2] S. Iijima, "Helical microtubules of graphitic carbon," *Nature*, vol. 354, pp. 56–58, 11 1991.
- [3] K. S. Novoselov, A. K. Geim, S. V. Morozov, D. Jiang, Y. Zhang, S. V. Dubonos, I. V. Grigorieva, and A. A. Firsov, "Electric Field Effect in Atomically Thin Carbon Films," *Science*, vol. 306, no. 5696, pp. 666–669, 2004.
- [4] K. S. Novoselov, Z. Jiang, Y. Zhang, S. V. Morozov, H. L. Stormer, U. Zeitler, J. C. Maan, G. S. Boebinger, P. Kim, and A. K. Geim, "Room-Temperature Quantum Hall Effect in Graphene," *Science*, vol. 315, no. 5817, p. 1379, 2007.
- [5] A. K. Geim and K. S. Novoselov, "The rise of graphene," *Nat. Mater.*, vol. 6, pp. 183–191, 03 2007.
- [6] K. S. Novoselov, A. K. Geim, S. V. Morozov, D. Jiang, M. I. Katsnelson, I. V. Grigorieva, S. V. Dubonos, and A. A. Firsov, "Two-dimensional gas of massless Dirac fermions in graphene," *Nature*, vol. 438, pp. 197–200, 11 2005.
- [7] K. S. Novoselov, E. McCann, S. V. Morozov, V. I. Fal'ko, M. I. Katsnelson, U. Zeitler, D. Jiang, F. Schedin, and A. K. Geim, "Unconventional quantum Hall effect and Berry's phase of 2π in bilayer graphene," *Nat. Phys.*, vol. 2, pp. 177–180, 03 2006.
- [8] C. Lee, X. Wei, J. W. Kysar, and J. Hone, "Measurement of the Elastic Properties and Intrinsic Strength of Monolayer Graphene," *Science*, vol. 321, no. 5887, pp. 385–388, 2008.
- [9] P. R. Wallace, "The Band Theory of Graphite," *Phys. Rev.*, vol. 71, pp. 622–634, May 1947.
- [10] Y. Zhang, Y.-W. Tan, H. L. Stormer, and P. Kim, "Experimental observation of the quantum Hall effect and Berry's phase in graphene," *Nature*, vol. 438, pp. 201–204, 11 2005.
- [11] K. I. Bolotin, F. Ghahari, M. D. Shulman, H. L. Stormer, and P. Kim, "Observation of the fractional quantum Hall effect in graphene," *Nature*, vol. 462, pp. 196–199, 11 2009.

- [12] M. I. Katsnelson, K. S. Novoselov, and A. K. Geim, “Chiral tunnelling and the Klein paradox in graphene,” *Nat. Phys.*, vol. 2, pp. 620–625, 09 2006.
- [13] P. Mallet, I. Brihuega, S. Bose, M. M. Ugeda, J. M. Gómez-Rodríguez, K. Kern, and J. Y. Veuillen, “Role of pseudospin in quasiparticle interferences in epitaxial graphene probed by high-resolution scanning tunneling microscopy,” *Phys. Rev. B*, vol. 86, p. 045444, Jul 2012.
- [14] I. Brihuega, P. Mallet, C. Bena, S. Bose, C. Michaelis, L. Vitali, F. Varchon, L. Magaud, K. Kern, and J.-Y. Veuillen, “Quasiparticle chirality in epitaxial graphene probed at the nanometer scale,” *Phys. Rev. Lett.*, vol. 101, no. 20, p. 206802, 2008.
- [15] K. K. Gomes, W. Mar, W. Ko, F. Guinea, and H. C. Manoharan, “Designer Dirac fermions and topological phases in molecular graphene,” *Nature*, vol. 483, pp. 306–310, 03 2012.
- [16] K. I. Bolotin, K. Sikes, Z. Jiang, M. Klima, G. Fudenberg, J. Hone, P. Kim, and H. Stormer, “Ultrahigh electron mobility in suspended graphene,” *Solid State Commun.*, vol. 146, no. 9, pp. 351–355, 2008.
- [17] M. Y. Han, B. Özyilmaz, Y. Zhang, and P. Kim, “Energy Band-Gap Engineering of Graphene Nanoribbons,” *Phys. Rev. Lett.*, vol. 98, p. 206805, May 2007.
- [18] Z. Chen, Y.-M. Lin, M. J. Rooks, and P. Avouris, “Graphene nano-ribbon electronics,” *Physica E*, vol. 40, no. 2, pp. 228–232, 2007.
- [19] L. A. Ponomarenko, F. Schedin, M. I. Katsnelson, R. Yang, E. W. Hill, K. S. Novoselov, and A. K. Geim, “Chaotic Dirac Billiard in Graphene Quantum Dots,” *Science*, vol. 320, no. 5874, pp. 356–358, 2008.
- [20] J. Cai, P. Ruffieux, R. Jaafar, M. Bieri, T. Braun, S. Blankenburg, M. Muoth, A. P. Seitsonen, M. Saleh, X. Feng, *et al.*, “Atomically precise bottom-up fabrication of graphene nanoribbons,” *Nature*, vol. 466, no. 7305, pp. 470–473, 2010.
- [21] J. van der Lit, M. P. Boneschanscher, D. Vanmaekelbergh, M. Ijäs, A. Upstu, M. Ervasti, A. Harju, P. Liljeroth, and I. Swart, “Suppression of electron–vibron coupling in graphene nanoribbons contacted via a single atom,” *Nat. Commun.*, vol. 4, 2013.
- [22] L. Jiao, L. Zhang, X. Wang, G. Diankov, and H. Dai, “Narrow graphene nanoribbons from carbon nanotubes,” *Nature*, vol. 458, no. 7240, pp. 877–880, 2009.
- [23] J. Coraux, M. Engler, C. Busse, D. Wall, N. Buckanie, F.-J. M. Zu Heringdorf, R. Van Gastel, B. Poelsema, T. Michely, *et al.*, “Growth of graphene on Ir (111),” *New J. Phys.*, vol. 11, no. 2, p. 023006, 2009.
- [24] S. Y. Zhou, G. H. Gweon, A. V. Fedorov, P. N. First, W. A. de Heer, D. H. Lee, F. Guinea, A. H. Castro Neto, and A. Lanzara, “Substrate-induced bandgap opening in epitaxial graphene,” *Nat. Mater.*, vol. 6, pp. 770–775, 10 2007.

- [25] G. Giovannetti, P. A. Khomyakov, G. Brocks, P. J. Kelly, and J. van den Brink, "Substrate-induced band gap in graphene on hexagonal boron nitride: *Ab initio* density functional calculations," *Phys. Rev. B*, vol. 76, p. 073103, Aug 2007.
- [26] B. Hunt, J. D. Sanchez-Yamagishi, A. F. Young, M. Yankowitz, B. J. LeRoy, K. Watanabe, T. Taniguchi, P. Moon, M. Koshino, P. Jarillo-Herrero, and R. C. Ashoori, "Massive Dirac Fermions and Hofstadter Butterfly in a van der Waals Heterostructure," *Science*, vol. 340, no. 6139, pp. 1427–1430, 2013.
- [27] S. Rusponi, M. Papagno, P. Moras, S. Vlaic, M. Etzkorn, P. M. Sheverdyayeva, D. Pacilé, H. Brune, and C. Carbone, "Highly Anisotropic Dirac Cones in Epitaxial Graphene Modulated by an Island Superlattice," *Phys. Rev. Lett.*, vol. 105, p. 246803, Dec 2010.
- [28] C.-H. Park, L. Yang, Y.-W. Son, M. L. Cohen, and S. G. Louie, "Anisotropic behaviours of massless Dirac fermions in graphene under periodic potentials," *Nat. Phys.*, vol. 4, pp. 213–217, 03 2008.
- [29] K. S. Novoselov, "Nobel lecture: Graphene: Materials in the flatland," *Rev. Mod. Phys.*, vol. 83, pp. 837–849, Aug 2011.
- [30] C. Oshima and A. Nagashima, "Ultra-thin epitaxial films of graphite and hexagonal boron nitride on solid surfaces," *J. Phys. Condens. Matter*, vol. 9, no. 1, p. 1, 1997.
- [31] J. Wintterlin and M.-L. Bocquet, "Graphene on metal surfaces," *Surf. Sci.*, vol. 603, no. 10–12, pp. 1841 – 1852, 2009. Special Issue of Surf. Sci. dedicated to Prof. Dr. Dr. h.c. mult. Gerhard Ertl, Nobel-Laureate in Chemistry 2007.
- [32] S.-T. Lee, S. Chen, G. Braunstein, X. Feng, I. Bello, and W. Lau, "Heteroepitaxy of carbon on copper by high-temperature ion implantation," *Appl. Phys. Lett.*, vol. 59, no. 7, pp. 785–787, 1991.
- [33] X. Li, W. Cai, J. An, S. Kim, J. Nah, D. Yang, R. Piner, A. Velamakanni, I. Jung, E. Tutuc, *et al.*, "Large-area synthesis of high-quality and uniform graphene films on copper foils," *Science*, vol. 324, no. 5932, pp. 1312–1314, 2009.
- [34] B. Nieuwenhuys, D. Hagen, G. Rovida, and G. Somorjai, "LEED, {AES} and thermal desorption studies of chemisorbed Hydrogen and hydrocarbons (C_2H_2 , C_2H_4 , C_6H_6 , C_6H_12) on the (111) and stepped $[6(111) \times (100)]$ iridium crystal surfaces; comparison with platinum," *Surf. Sci.*, vol. 59, no. 1, pp. 155 – 176, 1976.
- [35] D. Starr, E. Pazhetnov, A. Stadnichenko, A. Boronin, and S. Shaikhutdinov, "Carbon films grown on Pt(111) as supports for model gold catalysts," *Surf. Sci.*, vol. 600, no. 13, pp. 2688 – 2695, 2006.
- [36] P. Sutter, J. T. Sadowski, and E. Sutter, "Graphene on Pt (111): Growth and substrate interaction," *Phys. Rev. B*, vol. 80, no. 24, p. 245411, 2009.
- [37] N. A. Vinogradov, A. A. Zakharov, V. Kocovski, J. Ruzs, K. A. Simonov, O. Eriksson, A. Mikkelsen, E. Lundgren, A. S. Vinogradov, N. Mårtensson,

- and A. B. Preobrajenski, "Formation and Structure of Graphene Waves on Fe(110)," *Phys. Rev. Lett.*, vol. 109, p. 026101, Jul 2012.
- [38] R. Rosei, M. De Crescenzi, F. Sette, C. Quaresima, A. Savoia, and P. Perfetti, "Structure of graphitic carbon on Ni(111): A surface extended-energy-loss fine-structure study," *Phys. Rev. B*, vol. 28, pp. 1161–1164, Jul 1983.
- [39] J. Hamilton and J. Blakely, "Carbon segregation to single crystal surfaces of Pt, Pd and Co," *Surf. Sci.*, vol. 91, no. 1, pp. 199 – 217, 1980.
- [40] Y. Murata, E. Starodub, B. Kappes, C. Ciobanu, N. Bartelt, K. McCarty, and S. Kodambaka, "Orientation-dependent work function of graphene on Pd (111)," *Appl. Phys. Lett.*, vol. 97, no. 14, p. 143114, 2010.
- [41] A. T. N'Diaye, S. Bleikamp, P. J. Feibelman, and T. Michely, "Two-Dimensional Ir Cluster Lattice on a Graphene Moiré on Ir(111)," *Phys. Rev. Lett.*, vol. 97, p. 215501, Nov 2006.
- [42] E. Miniussi, M. Pozzo, A. Baraldi, E. Vesselli, R. R. Zhan, G. Comelli, T. O. Mentes, M. A. Niño, A. Locatelli, S. Lizzit, and D. Alfè, "Thermal Stability of Corrugated Epitaxial Graphene Grown on Re(0001)," *Phys. Rev. Lett.*, vol. 106, p. 216101, May 2011.
- [43] C. Tonnoir, A. Kimouche, J. Coraux, L. Magaud, B. Delsol, B. Gilles, and C. Chapelier, "Induced Superconductivity in Graphene Grown on Rhenium," *Phys. Rev. Lett.*, vol. 111, p. 246805, Dec 2013.
- [44] J. Grant and T. Haas, "A study of Ru(0001) and Rh(111) surfaces using (LEED) and Auger electron spectroscopy," *Surf. Sci.*, vol. 21, no. 1, pp. 76 – 85, 1970.
- [45] M.-C. Wu, Q. Xu, and D. W. Goodman, "Investigations of Graphitic Overlayers Formed from Methane Decomposition on Ru(0001) and Ru(111) Catalysts with Scanning Tunneling Microscopy and High-Resolution Electron Energy Loss Spectroscopy," *J. Phys. Chem.*, vol. 98, no. 19, pp. 5104–5110, 1994.
- [46] S. Marchini, S. Günther, and J. Winterlin, "Scanning tunneling microscopy of graphene on Ru(0001)," *Phys. Rev. B*, vol. 76, p. 075429, Aug 2007.
- [47] A. B. Preobrajenski, M. L. Ng, A. S. Vinogradov, and N. Mårtensson, "Controlling graphene corrugation on lattice-mismatched substrates," *Phys. Rev. B*, vol. 78, p. 073401, Aug 2008.
- [48] J. Vaari, J. Lahtinen, and P. Hautojärvi, "The adsorption and decomposition of acetylene on clean and K-covered Co(0001)," *Catal. Lett.*, vol. 44, no. 1-2, pp. 43–49, 1997.
- [49] A. Varykhalov and O. Rader, "Graphene grown on Co(0001) films and islands: Electronic structure and its precise magnetization dependence," *Phys. Rev. B*, vol. 80, p. 035437, Jul 2009.
- [50] J.-H. Lee, E. K. Lee, W.-J. Joo, Y. Jang, B.-S. Kim, J. Y. Lim, S.-H. Choi, S. J. Ahn, J. R. Ahn, M.-H. Park, C.-W. Yang, B. L. Choi, S.-W. Hwang, and D. Whang, "Wafer-Scale Growth of Single-Crystal Monolayer Graphene on Reusable Hydrogen-Terminated Germanium," *Science*, 2014.

- [51] X. Ding, G. Ding, X. Xie, F. Huang, and M. Jiang, "Direct growth of few layer graphene on hexagonal boron nitride by chemical vapor deposition," *Carbon*, vol. 49, no. 7, pp. 2522–2525, 2011.
- [52] S. Roth, F. Matsui, T. Greber, and J. Osterwalder, "Chemical Vapor Deposition and Characterization of Aligned and Incommensurate Graphene/Hexagonal Boron Nitride Heterostack on Cu(111)," *Nano Lett.*, vol. 13, no. 6, pp. 2668–2675, 2013.
- [53] I. Pletikosić, M. Kralj, P. Pervan, R. Brako, J. Coraux, A. T. N'Diaye, C. Busse, and T. Michely, "Dirac Cones and Minigaps for Graphene on Ir(111)," *Phys. Rev. Lett.*, vol. 102, p. 056808, Feb 2009.
- [54] J. Coraux, A. T. N'Diaye, C. Busse, and T. Michely, "Structural coherency of graphene on Ir (111)," *Nano Lett.*, vol. 8, no. 2, pp. 565–570, 2008.
- [55] R. Van Gastel, A. N'Diaye, D. Wall, J. Coraux, C. Busse, N. Buckanie, F.-J. M. Zu Heringdorf, M. H. von Hoegen, T. Michely, and B. Poelsema, "Selecting a single orientation for millimeter sized graphene sheets," *Appl. Phys. Lett.*, vol. 95, no. 12, p. 121901, 2009.
- [56] T. S. Marinova and D. Chakarov, "Adsorption of ethylene on Ir(111)," *Surf. Sci.*, vol. 192, no. 1, pp. 275–282, 1987.
- [57] T. S. Marinova and K. Kostov, "Adsorption of acetylene and ethylene on a clean Ir (111) surface," *Surf. Sci.*, vol. 181, no. 3, pp. 573–585, 1987.
- [58] J. Coraux, T. N. Plasa, C. Busse, T. Michely, *et al.*, "Structure of epitaxial graphene on Ir (111)," *New J. Phys.*, vol. 10, no. 4, p. 043033, 2008.
- [59] K. Hermann, "Periodic overlayers and moiré patterns: theoretical studies of geometric properties," *J. Phys. Condens. Matter*, vol. 24, no. 31, p. 314210, 2012.
- [60] M. Yankowitz, J. Xue, D. Cormode, J. D. Sanchez-Yamagishi, K. Watanabe, T. Taniguchi, P. Jarillo-Herrero, P. Jacquod, and B. J. LeRoy, "Emergence of superlattice Dirac points in graphene on hexagonal boron nitride," *Nat. Phys.*, vol. 8, no. 5, pp. 382–386, 2012.
- [61] G. Binnig, H. Rohrer, C. Gerber, and E. Weibel, " 7×7 Reconstruction on Si(111) Resolved in Real Space," *Phys. Rev. Lett.*, vol. 50, pp. 120–123, Jan 1983.
- [62] G. Binnig and H. Rohrer, "Scanning tunneling microscopy," *Helv. Phys. Acta*, vol. 55, no. 6, pp. 726–735, 1982.
- [63] G. Binnig, H. Rohrer, C. Gerber, and E. Weibel, "Tunneling through a controllable vacuum gap," *Appl. Phys. Lett.*, vol. 40, no. 2, pp. 178–180, 1982.
- [64] N. D. Lang, "Spectroscopy of single atoms in the scanning tunneling microscope," *Phys. Rev. B*, vol. 34, pp. 5947–5950, Oct 1986.
- [65] J. A. Stroscio, R. M. Feenstra, and A. P. Fein, "Electronic Structure of the Si(111) 2×1 Surface by Scanning-Tunneling Microscopy," *Phys. Rev. Lett.*, vol. 57, pp. 2579–2582, Nov 1986.
- [66] R. Feenstra, J. A. Stroscio, and A. Fein, "Tunneling spectroscopy of the Si (111) 2×1 surface," *Surf. Sci.*, vol. 181, no. 1, pp. 295–306, 1987.

- [67] W. Krenner, D. Kühne, F. Klappenberger, and J. V. Barth, “Assessment of Scanning Tunneling Spectroscopy Modes Inspecting Electron Confinement in Surface-Confined Supramolecular Networks,” *Sci. Rep.*, vol. 3, 03 2013.
- [68] T. Albrecht, P. Grütter, D. Horne, and D. Rugar, “Frequency modulation detection using high-Q cantilevers for enhanced force microscope sensitivity,” *J. Appl. Phys.*, vol. 69, no. 2, pp. 668–673, 1991.
- [69] J. N. Israelachvili, *Intermolecular and surface forces: revised third edition*. Academic press, 2011.
- [70] F. J. Giessibl, “A direct method to calculate tip-sample forces from frequency shifts in frequency-modulation atomic force microscopy,” *Appl. Phys. Lett.*, vol. 78, no. 1, pp. 123–125, 2001.
- [71] F. J. Giessibl, “High-speed force sensor for force microscopy and profilometry utilizing a quartz tuning fork,” *Appl. Phys. Lett.*, vol. 73, no. 26, pp. 3956–3958, 1998.
- [72] F. J. Giessibl, “Atomic resolution on Si (111)-(7 × 7) by noncontact atomic force microscopy with a force sensor based on a quartz tuning fork,” *Appl. Phys. Lett.*, vol. 76, no. 11, pp. 1470–1472, 2000.
- [73] S. Morita, R. Wiesendanger, and E. Meyer, *Noncontact atomic force microscopy*, vol. 1. Springer, 2002.
- [74] K. Oura, A. Zotov, V. Lifshits, A. Saranin, and M. Katayama, *Surface Science*. Springer, 2003.
- [75] S. Andersson and B. Kasemo, “Low-energy electron diffraction intensities from the clean nickel (001) surface,” *Surf. Sci.*, vol. 25, no. 2, pp. 273–288, 1971.
- [76] K. Christmann, G. Ertl, and O. Schöber, “LEED intensities from clean and hydrogen covered Ni (100) and Pd (111) surfaces,” *Surf. Sci.*, vol. 40, no. 1, pp. 61–70, 1973.
- [77] A. T. Hubbard, *The Handbook of surface imaging and visualization*. CRC Press, 1995.
- [78] J. Pendry, “Reliability factors for LEED calculations,” *J. Phys. C: Solid State Phys.*, vol. 13, no. 5, p. 937, 1980.
- [79] F. Jean, T. Zhou, N. Blanc, R. Felici, J. Coraux, and G. Renaud, “Effect of preparation on the commensurabilities and thermal expansion of graphene on Ir(111) between 10 and 1300 K,” *Phys. Rev. B*, vol. 88, p. 165406, Oct 2013.
- [80] N. Blanc, J. Coraux, C. Vo-Van, A. T. N’Diaye, O. Geaymond, and G. Renaud, “Local deformations and incommensurability of high-quality epitaxial graphene on a weakly interacting transition metal,” *Phys. Rev. B*, vol. 86, p. 235439, Dec 2012.
- [81] H. Hattab, A. T. N’Diaye, D. Wall, C. Klein, G. Jnawali, J. Coraux, C. Busse, R. van Gastel, B. Poelsema, T. Michely, *et al.*, “Interplay of wrinkles, strain, and lattice parameter in graphene on iridium,” *Nano Lett.*, vol. 12, no. 2, pp. 678–682, 2012.

- [82] E. N. Voloshina, E. Fertitta, A. Garhofer, F. Mittendorfer, M. Fonin, A. Thissen, and Y. S. Dedkov, “Electronic structure and imaging contrast of graphene moire on metals,” *Sci. Rep.*, vol. 3, 2013.
- [83] C. Busse, P. Lazić, R. Djemour, J. Coraux, T. Gerber, N. Atodiresci, V. Caciuc, R. Brako, A. T. N’Diaye, S. Blügel, J. Zegenhagen, and T. Michely, “Graphene on Ir(111): Physisorption with Chemical Modulation,” *Phys. Rev. Lett.*, vol. 107, p. 036101, Jul 2011.
- [84] J. Sławińska, P. Dabrowski, and I. Zasada, “Doping of graphene by a Au(111) substrate: Calculation strategy within the local density approximation and a semiempirical van der Waals approach,” *Phys. Rev. B*, vol. 83, p. 245429, Jun 2011.
- [85] M. Vanin, J. J. Mortensen, A. Kelkkanen, J. M. Garcia-Lastra, K. S. Thygesen, and K. W. Jacobsen, “Graphene on metals: A van der Waals density functional study,” *Phys. Rev. B*, vol. 81, no. 8, p. 081408, 2010.
- [86] M. Iannuzzi, F. Tran, R. Widmer, T. Dienel, K. Radican, Y. Ding, J. Hutter, and O. Gröning, “Site-selective adsorption of phthalocyanine on h-BN/Rh (111) nanomesh,” *Phys. Chem. Chem. Phys.*, 2014.
- [87] Y. Dedkov and E. Voloshina, “Multichannel scanning probe microscopy and spectroscopy of graphene moiré structures,” *Phys. Chem. Chem. Phys.*, 2014.
- [88] M. P. Boneschanscher, J. van der Lit, Z. Sun, I. Swart, P. Liljeroth, and D. Vanmaekelbergh, “Quantitative atomic resolution force imaging on epitaxial graphene with reactive and nonreactive AFM probes,” *ACS nano*, vol. 6, no. 11, pp. 10216–10221, 2012.
- [89] L. Gross, F. Mohn, N. Moll, P. Liljeroth, and G. Meyer, “The Chemical Structure of a Molecule Resolved by Atomic Force Microscopy,” *Science*, vol. 325, no. 5944, pp. 1110–1114, 2009.
- [90] P. Liljeroth, I. Swart, S. Paavilainen, J. Repp, and G. Meyer, “Single-Molecule Synthesis and Characterization of Metal- Ligand Complexes by Low-Temperature STM,” *Nano Lett.*, vol. 10, no. 7, pp. 2475–2479, 2010.
- [91] I. Swart, L. Gross, and P. Liljeroth, “Single-molecule chemistry and physics explored by low-temperature scanning probe microscopy,” *Chem. Commun.*, vol. 47, no. 32, pp. 9011–9023, 2011.
- [92] L. Gross, F. Mohn, N. Moll, B. Schuler, A. Criado, E. Guitián, D. Peña, A. Gourdon, and G. Meyer, “Bond-Order Discrimination by Atomic Force Microscopy,” *Science*, vol. 337, no. 6100, pp. 1326–1329, 2012.
- [93] D. G. de Oteyza, P. Gorman, Y.-C. Chen, S. Wickenburg, A. Riss, D. J. Mowbray, G. Etkin, Z. Pedramrazi, H.-Z. Tsai, A. Rubio, M. F. Crommie, and F. R. Fischer, “Direct Imaging of Covalent Bond Structure in Single-Molecule Chemical Reactions,” *Science*, vol. 340, no. 6139, pp. 1434–1437, 2013.
- [94] L. Bartels, G. Meyer, and K.-H. Rieder, “Controlled vertical manipulation of single CO molecules with the scanning tunneling microscope: A route to chemical contrast,” *Appl. Phys. Lett.*, vol. 71, no. 2, pp. 213–215, 1997.

- [95] E. Niemi and J. Nieminen, “Molecular reorientation in assembled CO structures and contrast inversion in STM,” *Chem. Phys. Lett.*, vol. 397, no. 1, pp. 200–204, 2004.
- [96] J. A. Nieminen, E. Niemi, and K.-H. Rieder, “Interference between competing tunneling channels and chemical resolution of STM,” *Surf. Sci.*, vol. 552, no. 1, pp. L47–L52, 2004.
- [97] W. Moritz, B. Wang, M.-L. Bocquet, T. Brugger, T. Greber, J. Wintterlin, and S. Günther, “Structure Determination of the Coincidence Phase of Graphene on Ru(0001),” *Phys. Rev. Lett.*, vol. 104, p. 136102, Apr 2010.
- [98] S. Runte, P. Lazić, C. Vo-Van, J. Coraux, J. Zegenhagen, and C. Busse, “Graphene buckles under stress: An x-ray standing wave and scanning tunneling microscopy study,” *Phys. Rev. B*, vol. 89, no. 15, p. 155427, 2014.
- [99] A. R. Akhmerov and C. W. J. Beenakker, “Boundary conditions for Dirac fermions on a terminated honeycomb lattice,” *Phys. Rev. B*, vol. 77, p. 085423, Feb 2008.
- [100] H. Heiskanen, M. Manninen, and J. Akola, “Electronic structure of triangular, hexagonal and round graphene flakes near the Fermi level,” *New J. Phys.*, vol. 10, no. 10, p. 103015, 2008.
- [101] E. Starodub, A. Bostwick, L. Moreschini, S. Nie, F. E. Gabaly, K. F. McCarty, and E. Rotenberg, “In-plane orientation effects on the electronic structure, stability, and Raman scattering of monolayer graphene on Ir(111),” *Phys. Rev. B*, vol. 83, p. 125428, Mar 2011.
- [102] S.-h. Phark, J. Borme, A. L. Vanegas, M. Corbetta, D. Sander, and J. Kirschner, “Direct observation of electron confinement in epitaxial graphene nanoislands,” *ACS nano*, vol. 5, no. 10, pp. 8162–8166, 2011.
- [103] D. Subramaniam, F. Libisch, Y. Li, C. Pauly, V. Geringer, R. Reiter, T. Mashoff, M. Liebmann, J. Burgdörfer, C. Busse, *et al.*, “Wave-function mapping of graphene quantum dots with soft confinement,” *Phys. Rev. Lett.*, vol. 108, no. 4, p. 046801, 2012.
- [104] S. Altenburg, J. Kröger, T. Wehling, B. Sachs, A. Lichtenstein, and R. Berndt, “Local gating of an Ir (111) surface resonance by graphene islands,” *Phys. Rev. Lett.*, vol. 108, no. 20, p. 206805, 2012.
- [105] A. Varykhalov, D. Marchenko, M. R. Scholz, E. D. L. Rienks, T. K. Kim, G. Bihlmayer, J. Sánchez-Barriga, and O. Rader, “Ir(111) Surface State with Giant Rashba Splitting Persists under Graphene in Air,” *Phys. Rev. Lett.*, vol. 108, p. 066804, Feb 2012.
- [106] Y. Zhang, V. W. Brar, F. Wang, C. Girit, Y. Yayon, M. Panlasigui, A. Zettl, and M. F. Crommie, “Giant phonon-induced conductance in scanning tunnelling spectroscopy of gate-tunable graphene,” *Nat. Phys.*, vol. 4, pp. 627–630, 08 2008.
- [107] L. Zhao, R. He, K. T. Rim, T. Schiros, K. S. Kim, H. Zhou, C. Gutiérrez, S. P. Chockalingam, C. J. Arguello, L. Pálová, D. Nordlund, M. S. Hybertsen, D. R. Reichman, T. F. Heinz, P. Kim, A. Pinczuk, G. W. Flynn, and A. N. Pasupathy, “Visualizing Individual Nitrogen Dopants in Monolayer Graphene,” *Science*, vol. 333, no. 6045, pp. 999–1003, 2011.

- [108] S. De Feyter and F. C. De Schryver, "Two-dimensional supramolecular self-assembly probed by scanning tunneling microscopy," *Chem. Soc. Rev.*, vol. 32, no. 3, pp. 139–150, 2003.
- [109] J. A. Elemans, R. van Hameren, R. J. Nolte, and A. E. Rowan, "Molecular Materials by Self-Assembly of Porphyrins, Phthalocyanines, and Perylenes," *Adv. Mater.*, vol. 18, no. 10, pp. 1251–1266, 2006.
- [110] R. Decker, Y. Wang, V. W. Brar, W. Regan, H.-Z. Tsai, Q. Wu, W. Gannett, A. Zettl, and M. F. Crommie, "Local electronic properties of graphene on a bn substrate via scanning tunneling microscopy," *Nano letters*, vol. 11, no. 6, pp. 2291–2295, 2011.
- [111] T. Gopakumar, M. Lackinger, M. Hackert, F. Müller, and M. Hietschold, "Adsorption of palladium phthalocyanine on graphite: STM and LEED study," *J. Phys. Chem. B*, vol. 108, no. 23, pp. 7839–7843, 2004.
- [112] X. Lu, K. W. Hipps, X. D. Wang, and U. Mazur, "Scanning Tunneling Microscopy of Metal Phthalocyanines: d⁷ and d⁹ cases," *J. Am. Chem. Soc.*, vol. 118, no. 30, pp. 7197–7202, 1996.
- [113] X. Chen, Y.-S. Fu, S.-H. Ji, T. Zhang, P. Cheng, X.-C. Ma, X.-L. Zou, W.-H. Duan, J.-F. Jia, and Q.-K. Xue, "Probing Superexchange Interaction in Molecular Magnets by Spin-Flip Spectroscopy and Microscopy," *Phys. Rev. Lett.*, vol. 101, p. 197208, Nov 2008.
- [114] J. Mao, H. Zhang, Y. Jiang, Y. Pan, M. Gao, W. Xiao, and H.-J. Gao, "Tunability of supramolecular kagome lattices of magnetic phthalocyanines using graphene-based moiré patterns as templates," *J. Am. Chem. Soc.*, vol. 131, no. 40, pp. 14136–14137, 2009.
- [115] Y. Zhang, V. W. Brar, C. Girit, A. Zettl, and M. F. Crommie, "Origin of spatial charge inhomogeneity in graphene," *Nat. Phys.*, vol. 5, pp. 722–726, 10 2009.
- [116] J. Martin, N. Akerman, G. Ulbricht, T. Lohmann, J. H. Smet, K. von Klitzing, and A. Yacoby, "Observation of electron-hole puddles in graphene using a scanning single-electron transistor," *Nat. Phys.*, vol. 4, pp. 144–148, 02 2008.
- [117] J. Xue, J. Sanchez-Yamagishi, D. Bulmash, P. Jacquod, A. Deshpande, K. Watanabe, T. Taniguchi, P. Jarillo-Herrero, and B. J. LeRoy, "Scanning tunnelling microscopy and spectroscopy of ultra-flat graphene on hexagonal boron nitride," *Nat. Mater.*, vol. 10, no. 4, pp. 282–285, 2011.
- [118] P. Järvinen, S. K. Hämäläinen, M. Ijäs, A. Harju, and P. Liljeroth, "Self-Assembly and Orbital Imaging of Metal Phthalocyanines on a Graphene Model Surface," *Submitted to J. Phys. Chem. C.*, 2014.

Errata

Publication I

Since the publication of this paper, it has become clear that the reactivity of the tip plays a role on the imaging contrast and hence AFM images acquired with metal tips cannot be directly interpreted as true surface topography on this graphene on Ir(111) system. This affects one of the conclusions of this publication, where the topography of the moiré pattern from the atomic force microscopy images was interpreted as the true topography. The measurements themselves and the modeling of the effect of the background forces on the AFM response are correct.



ISBN 978-952-60-5886-3
ISBN 978-952-60-5887-0 (pdf)
ISSN-L 1799-4934
ISSN 1799-4934
ISSN 1799-4942 (pdf)

Aalto University
School of Science
Department of Applied Physics
www.aalto.fi

**BUSINESS +
ECONOMY**

**ART +
DESIGN +
ARCHITECTURE**

**SCIENCE +
TECHNOLOGY**

CROSSOVER

**DOCTORAL
DISSERTATIONS**